

TEMPERATURE TOMOGRAPHY OF THE SOFT X-RAY CORONA: MEASUREMENTS OF ELECTRON DENSITIES, TEMPERATURES, AND DIFFERENTIAL EMISSION MEASURE DISTRIBUTIONS ABOVE THE LIMB

MARKUS J. ASCHWANDEN

Lockheed Martin Advanced Technology Center, Solar and Astrophysics Laboratory, Department L9-41, Building 252, 3251 Hanover Street, Palo Alto, CA 94304; aschwanden@lmsal.com

AND

LOREN W. ACTON

Montana State University, Bozeman, MT 59717
 Received 2000 May 4; accepted 2000 November 20

ABSTRACT

We analyze long-exposure and off-pointing *Yohkoh*/SXT data of the solar corona observed on 1992 August 26. We develop a new (temperature) tomography method that is based on a forward-fitting method of a four-parameter model to the observed soft X-ray fluxes $F_1(h)$ and $F_2(h)$ of two SXT wavelength filters as a function of height h . The model is defined in terms of a differential emission measure (DEM) distribution $dEM(h, T)/dT$, which includes also a temperature dependence of density scale heights $\lambda_n(T) = q_\lambda \lambda_T$ and allows us to quantify deviations ($q_\lambda \neq 1$) from hydrostatic equilibrium ($q_\lambda = 1$). This parametrization facilitates a proper line-of-sight integration and relates the widely used filter ratio temperature T_{FR} to the peak of the DEM distribution. A direct consequence of the multi-scale height atmosphere is that the filter ratio temperature $T_{FR}(h)$ is predicted to increase with height, even if all magnetic field lines are isothermal. Our model fitting reveals that coronal holes and quiet-Sun regions are in perfect hydrostatic equilibrium but that coronal streamers have a scale height that exceeds the hydrostatic scale height by a factor of up to $q_\lambda \lesssim 2.3$, which underscores the dynamic nature of coronal streamers. Our density measurements in coronal holes are slightly lower than most of the white-light polarized brightness inversions and seem to come closer to the requirements of solar wind models. Our DEM model provides also a physical framework for the semiempirical Baumbach-Allen formula and quantifies the temperature ranges and degree of hydrostaticity of the K, L, and F coronae.

Subject headings: Sun: atmosphere — Sun: corona — Sun: X-rays, gamma rays

1. INTRODUCTION

Large-scale physical properties of the solar corona, such as electron density, temperature, velocity, and magnetic field, represent fundamental quantities needed to solve the problems of coronal heating and solar wind acceleration. A major effort in this direction has recently been undertaken with the Whole Sun Month Campaign (Galvin & Kohl 1999). The comparison of such multiwavelength data sets often reveals significant differences in coronal temperature measurements. For example, these discrepancies clearly demonstrate that electron densities and temperatures cannot be modeled separately but need to be synthesized with coupled, self-consistent functions. Here we explore a new method that may be called temperature tomography because a three-dimensional density distribution is reconstructed from images in multiple temperatures, in analogy to classical tomography based on images from multiple aspect angles. For this approach we employ forward-fitting of a combined coronal density and temperature model to observed fluxes in soft X-ray (SXR) wavelengths, using a well-suited quiet-Sun observation (Acton & Lemen 1998) from the *Yohkoh* soft X-ray telescope (SXT; Tsuneta et al. 1991). Our physical model includes a description of the electron density $n_e(T_e)$ as function of temperature T_e in the form of a differential emission measure (DEM) distribution, constrained by the line-of-sight integration in an inhomogeneous atmosphere with parametrized scale heights. Such a tomographic method is applied to soft X-ray data of the quiet Sun, apparently for the first time. Previous soft X-ray

studies on the quiet Sun using *Yohkoh*/SXT data did not take DEM temperature distributions into account (e.g., Sturrock, Wheatland, & Acton 1996; Wheatland, Sturrock, & Acton 1997; Alexander 1999; Wolfson et al. 2000).

Traditionally, the density structure of the large-scale corona is probed from white-light (polarized brightness) data using a van de Hulst (1950a, 1950b) inversion. The van de Hulst method assumes that the polarized brightness of white light is produced by Thomson scattering and is proportional to the line-of-sight integrated coronal electron density. The polarized brightness of the three different coronal components seen in white light (K, L, and F coronae) can then be inverted by a power-law *Ansatz* as a function of the Sun center distance R , i.e., $pB(R) = \sum_{i=1}^3 a_i R^{-b_i}$, assuming that the radial density gradient is steeper than the transverse gradient (van de Hulst 1950a, 1950b). A temperature can only be derived in this model with the two assumptions of hydrostatic equilibrium and isothermality (along each line of sight; for a recent application see, e.g., Gibson et al. 1999). This approach neglects the multitemperature structure of the solar corona, as it is blatantly evident from soft X-ray and EUV observations, and ignores the corresponding multi-scale height effects in the line-of-sight integration of the densities (Aschwanden & Nitta 2000). The isothermal approach therefore leads to radial temperature profiles $T_e(h)$ that are inconsistent with those derived from multitemperature models (based on DEM distributions). Consequently, conflicting temperature comparisons were reported in multiwavelength studies,

when the various temperatures inferred from different instruments and wavelengths were not modeled with a common DEM distribution (e.g., Gibson et al. 1999; Fludra et al. 1999; Wolfson et al. 2000). We will show in this study that the discrepant temperature profiles $T_e(h)$ inferred from different wavelengths can be reconciled by proper consideration of the DEM distribution in a multi-scale height atmosphere.

The content of this paper includes a formulation of a quiet-Sun model based on a DEM distribution and related scale height parametrization (§ 2), the fitting of this model to quiet-Sun data observed with *Yohkoh*/SXT (§ 3), a description of quantitative results (§ 4), a discussion of the results, comparisons with previous coronal density and temperature measurements (§ 5), and conclusions (§ 6).

2. MODEL PARAMETERIZATION

2.1. Differential Emission Measure

We measure the soft X-ray flux of the solar corona above the limb in two filters, averaged over macropixels with a size of $\approx 20''$. Because of the broadband temperature response of the *Yohkoh* SXT, the line-of-sight integration, and the averaging over large spatial volumes, it is appropriate to characterize the coronal plasma with a multitemperature distribution at any spatial position $x = (x, y, z)$. For this purpose we define a differential electron density distribution $dn_e(x, T)/dT$, characterized by a Gaussian as a function of temperature,

$$\frac{dn_e(x, T)}{dT} = \frac{n_e(x)}{\sqrt{2\pi}\sigma_T} \exp\left[-\frac{(T - T_0)^2}{2\sigma_T^2}\right]. \quad (1)$$

This temperature distribution is characterized by three parameters: the total electron density $n_e(x)$, the mean electron temperature T_0 , and the Gaussian temperature distribution width σ_T . The differential electron density distribution is normalized so that the integral over the entire temperature range yields the total electron density $n_e(x)$ at a spatial location x ,

$$\int \left[\frac{dn_e(x, T)}{dT} \right] dT = n_e(x). \quad (2)$$

We define the corresponding DEM distribution integrated along a line of sight z ,

$$\begin{aligned} \frac{dEM(x, y, T)}{dT} &= \int \left[\frac{dn_e(x, T)}{dT} \right]^2 2\sqrt{\pi}\sigma_T dz \\ &= \int \frac{n_e^2(x)}{\sqrt{\pi}\sigma_T} \exp\left[-\frac{(T - T_0)^2}{\sigma_T^2}\right] dz, \end{aligned} \quad (3)$$

which contains a normalization factor so that the total emission measure (EM), obtained by integrating over the entire temperature range, meets the standard definition of column emission measure,

$$EM(x, y) = \int \left[\frac{dEM(x, y, T)}{dT} \right] dT = \int n_e^2(x) dz. \quad (4)$$

Implicitly, we assume here that the ion density is equal to the electron density, $n_i = n_e$, because the general definition of the DEM is $dEM(T)/dT \propto n_i n_e dV$.

The (x, y) -plane represents the image plane in the plane of sky, with the origin $x = (0, 0, 0)$ at Sun center, while the

z -direction corresponds to the line of sight of the observer. In this study we will consider mainly the height dependence of the DEM distribution, $dEM(h, T)/dT$, where the height is defined by $h = (x^2 + y^2 + z^2)^{1/2} - r_\odot$, with $r_\odot = 696$ Mm being the solar radius.

2.2. Hydrostatic Scaling

The coronal plasma is expected to be in hydrostatic equilibrium, at least in the long-time average. The hydrostatic scale height λ_T is proportional to the electron temperature T for an isothermal structure, i.e.,

$$\lambda_T = \frac{k_B T}{\mu m_p g_\odot} = \lambda_0 \left(\frac{T}{1 \text{ MK}} \right), \quad (5)$$

with $\lambda_0 = 47$ Mm for coronal conditions, where μm_p is the average ion mass (i.e., $\mu \approx 1.3$ for H:He = 10:1) and g_\odot is the solar gravitation. The height dependence of the electron density is thus

$$n_e(h, T) = n_e(h_0) \exp\left[-\frac{(h - h_0)}{q_\lambda \lambda_0 T}\right], \quad (6)$$

where $q_\lambda = \lambda_n/\lambda_T$ represents the ratio of the observed density scale height λ_n to the temperature scale height $\lambda_T = \lambda_0 T$ and thus allows us to quantify deviations from the hydrostatic equilibrium ($q_\lambda = 1$). This hydrostatic height dependence leads to a variation of the DEM distribution with height. We show (in Fig. 1) the resulting DEM distributions as a function of height ($h = 0, 50, 100, 150, 200$ Mm) for two corona components: (1) a quiet-Sun region with a temperature distribution that peaks at $T_{\max} = 1.5$ Mm and has a width of $\sigma_T = 0.5$ MK [with base density $n_e(h_0) = 10^8 \text{ cm}^{-3}$ and a column depth corresponding to the line-of-sight integration across a plane-parallel corona] and (2) an active region with a temperature distribution of $T_{\max} = 4.5$ Mm and $\sigma_T = 1.5$ MK (with the same base density and a half column depth of $D = 150$ Mm). Note that the peaks of the DEM distributions have a decreasing emission measure with height and a shift toward higher temperatures (Fig. 1, top panel).

The variation of the electron density $n_e(h)$ as a function of height h is obtained by integrating over the temperature range (eq. [2]),

$$\begin{aligned} n_e(h) &= \int \left[\frac{dn_e(h, T)}{dT} \right] dT \\ &= \int \frac{n_e(h_0)}{\sqrt{2\pi}\sigma_T} \exp\left[-\frac{(h - h_0)}{q_\lambda \lambda_0 T} - \frac{(T - T_0)^2}{2\sigma_T^2}\right] dT, \end{aligned} \quad (7)$$

which can easily be calculated by numerical integration. The density height profile $n_e(h)$ would be exactly an exponential function for an isothermal atmosphere ($\sigma_T \ll T_0$) but falls off less steeply with progressing height for a multithermal atmosphere ($\sigma_T \approx T_0$).

2.3. Line-of-Sight Integration

To model the diffuse corona observed above the limb, we start with the simplest three-dimensional model, i.e., a spherically symmetric density distribution with a radial dependence according to the hydrostatic scaling $n_e(h, T)$ (eq. [6]), but having a fine structure with a distribution of temperatures that is characterized by the differential electron density distribution $dn_e(x, T)/dT$ (eq. [1]) at the coronal base ($h = h_0$). Denoting the direction of the line of sight

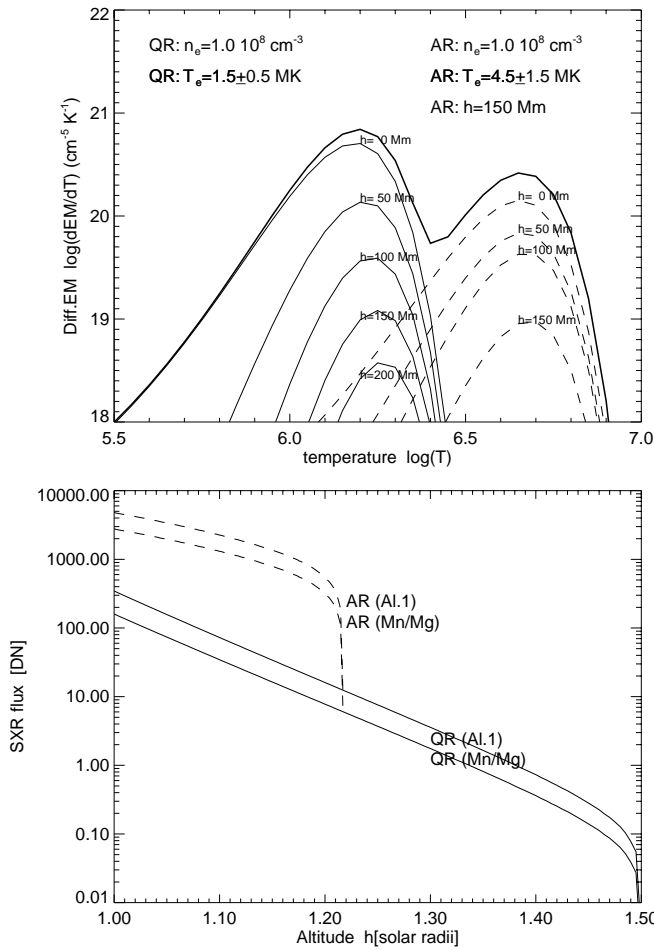


FIG. 1.—Model DEM distributions $dEM(h, T)/dT$ are calculated (top panel) for a quiet-Sun (QR) component (solid lines, $n_e = 10^8 \text{ cm}^{-3}$, $T_e = 1.5 \text{ MK}$, $\sigma_T = 0.5 \text{ MK}$) and for an active region with an extent of $R = D = 150 \text{ Mm}$ (dashed lines, $n_e = 10^8 \text{ cm}^{-3}$, $T_e = 4.5 \text{ MK}$, $\sigma_T = 1.5 \text{ MK}$). Each distribution is shown for different heights above the limb ($h = 0, 50, 100, 150$, and 200 Mm). The corresponding soft X-ray fluxes for the *Yohkoh*/SXT filters Al.1 and Mn/Mg are shown as a function of height in the bottom panel (for half-resolution pixels of $4''.9$ and an exposure time of $t_{\text{exp}} = 247.164 \text{ s}$). Note that the hotter component produces a soft X-ray flux profile $F(h)$ with a flatter slope.

with z , a simple geometric consideration yields the following height dependence $h'(z)$ for a point z on the line-of-sight axis that passes the limb at a lowest height h (at location $z = 0$):

$$h'(z) = \sqrt{(r_\odot + h)^2 + z^2} - r_\odot \quad (8)$$

(see Fig. 2). Combining equation (8) with equations (3)–(6), we obtain then the following differential emission measure $dEM(h, T)/dT$ for a position h above the limb, integrated along the line of sight z :

$$\begin{aligned} \frac{dEM(h, T)}{dT} &= \int_{-\infty}^{\infty} \frac{n_e^2(h_0)}{\sqrt{\pi} \sigma_T} \\ &\times \exp \left\{ -\frac{2[h'(z) - h_0]}{q_\lambda \lambda_0 T} - \frac{(T - T_0)^2}{\sigma_T^2} \right\} dz. \end{aligned} \quad (9)$$

Multiplying the DEM distribution $dEM(h, T)/dT$ with the instrumental response function $R_W(T) = dF_W/dEM(T)$ of a

filter with wavelength W and integrating over the temperature range, we obtain then directly the flux $F_W(h)$ at a given height h :

$$\begin{aligned} F_W(h) &= \int_0^\infty \frac{dF_W(h)}{dEM(h, T)} \frac{dEM(h, T)}{dT} dT \\ &= \int_0^\infty R_W(T) \frac{dEM(h, T)}{dT} dT. \end{aligned} \quad (10)$$

2.4. Column Depth

It is instructive to visualize the column depth of a hydrostatically stratified atmosphere as a function of the distance to Sun center because the electron density can then directly be estimated from this column depth and an observed emission measure. We define an equivalent column depth along the line of sight, $z_{\text{eq}}(h, T)$, as a function of the height h above the limb and for a coronal temperature T_0 (in the isothermal approximation $\sigma_{T_0} \ll T_0$),

$$EM(h, T_0) = \int_{-\infty}^{\infty} n_e^2(h, z, T_0) dz = n_e^2(h_0, T_0) z_{\text{eq}}(h, T_0). \quad (11)$$

From equations (4)–(9) the following relation follows for this equivalent column depth (for $q_\lambda = 1$):

$$z_{\text{eq}}(h, T_0) = \int_{z_1}^{z_2} \exp \left\{ -\frac{2}{\lambda_0 T_0} [\sqrt{(r_\odot + h)^2 + z^2} - r_\odot] \right\} dz \quad (12)$$

for $h \geq 0$, with the integration limits $z_1 = -\infty$ and $z_2 = \infty$. Inside the disk ($-1 \leq h \leq 0$) we have only to change the integration limit z_2 to

$$z_2(h) = -\sqrt{r_\odot^2 - (r_\odot + h)^2} \quad \text{for } -1 < h < 0. \quad (13)$$

The column depths $z_{\text{eq}}(h, T_0)$ are shown in Figure 3 for a height range from disk center ($h = -1$) to one solar radius outside the limb ($h = 1$), for temperatures in the range of $T = 1.0$ – 4.0 MK . At disk center ($h = -1$), the equivalent column depth matches the emission measure scale height, which is half the density scale height ($\lambda_{\text{EM}} = \lambda_n/2 = \lambda_0 T_0/2$) (Fig. 3, dashed lines). At the limb ($h = 0$), there is in principle a discontinuous change by a factor of 2, which, however, is difficult to measure because of the extremely high instrumental resolution required to resolve this jump. Above the limb, the column depth drops quickly with height. This dependence of the column depth on the Sun center distance constrains the soft X-ray brightness across and outside the solar disk.

2.5. Closed-Field Geometry

The previously described model assumes the simplest geometry, i.e., vertically oriented open flux tubes with radial expansion factors. However, active regions, coronal streamers, or arcades of loops demarcate regions with closed-field lines that can confine plasma with a different temperature distribution. In order to accommodate such regions to first order, we can characterize such regions with an elliptical geometry, having a radius R perpendicular to the line of sight and a half-depth D parallel to the line of sight. For an arbitrary height h above the limb, the line-of-sight extent of such a structure is (see Fig. 2, bottom panel)

$$|z(h)| \leq z_1 = \left(\frac{D}{R}\right) \sqrt{R^2 - h^2} \quad (h < R). \quad (14)$$

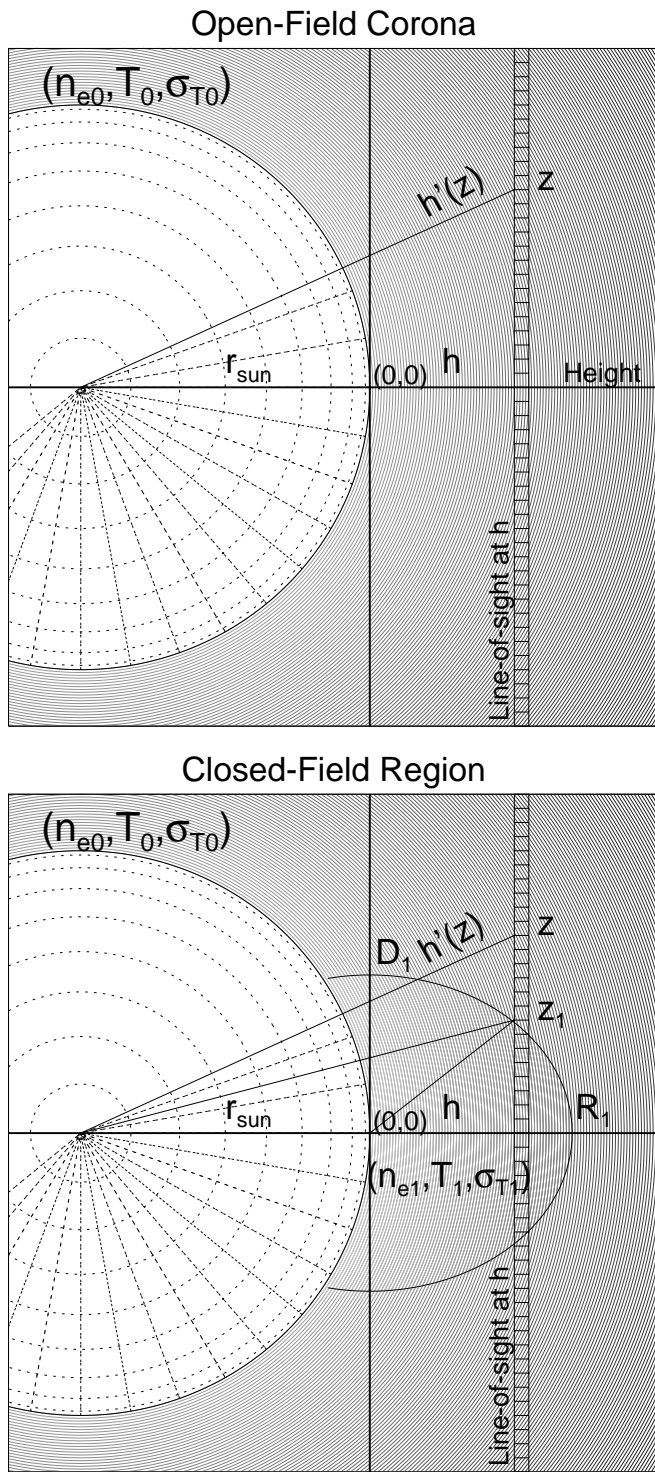


FIG. 2.—Geometric definitions are shown in a plane along the line of sight, for the open-field corona (*top panel*) and for an additional closed-field region (*bottom panel*). The height as a function of the line-of-sight distance z is denoted with $h(z)$. The extent of the closed-field region has a height of R_1 perpendicular to the line of sight and a half-depth of D_1 parallel to the line of sight.

This way, we can generalize our model of the quiet-Sun emission to two components (Fig. 2, *bottom panel*): (1) open-field regions with radial structures and (2) closed-field regions, confined to an elliptical geometry with half-axes of R and D , centered at limb position ($h = 0, z = 0$). Open-field regions (denoted with subscript 0) require then four free

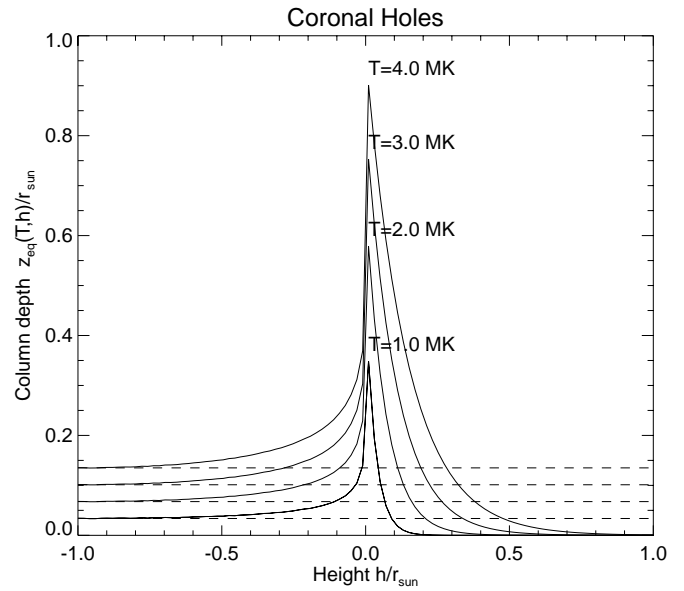


FIG. 3.—Calculated equivalent column depths $z_{eq}(T, h)$ (eq. [12]) for a gravitationally stratified atmosphere as a function of the limb distance h , for isothermal plasmas with temperatures of column depths, correspond to the emission measure scale heights (i.e., half the density scale height) for vertical lines of sight at Sun center ($h/r_{\odot} = -1$), indicated with dashed lines.

parameters ($n_0, T_0, \sigma_{T0}, q_{\lambda 0}$), while closed-field regions (denoted with subscript 1) require six additional parameters ($n_1, T_1, \sigma_{T1}, q_{\lambda 1}, R_1, D_1$). The line-of-sight integration (eq. [9]) is then simply composed of two parts,

$$\frac{dEM(h, T)}{dT} = 2 \int_0^{z_1(h, R_1, D_1)} f(n_1, T_1, \sigma_{T1}, q_{\lambda 1}) dz + 2 \int_{z_1(h, R_1, D_1)}^{\infty} f(n_0, T_0, \sigma_{T0}, q_{\lambda 0}) dz, \quad (15)$$

where the function $f(\dots)$ stands for the expressions inside the integral in equation (9).

3. DATA ANALYSIS

3.1. Observations

The data set of quiet-Sun observations obtained with the *Yohkoh* SXT (Tsuneta et al. 1991) that we are using is unique in three aspects: (1) it contains long-exposure images that provide a high signal-to-noise ratio, (2) it contains images with off-disk pointings that scan the brightness of the solar corona far out to $\lesssim 1.8 r_{\odot}$, and (3) the instrument has a minimum of stray light (before the rupture of the entrance filter in 1992 November). This data set is therefore optimally suited to analyze the physical parameters of the quiet Sun far out to the faintest soft X-ray emission in the outermost parts of the solar corona and has been previously described by Acton & Lemen (1998).

The data were taken on 1992 August 26 between 20:45 UT and 22:59 UT, consisting of a sequence of 16 exposures, with eight in the thin aluminum (Al1) and eight in the composite filter (Al/Mg/Mn). The sequence contains two long-exposure images (60.418 s), one medium-exposure image (2.668 s), and one short-exposure image (0.078 s) through each filter and for each off-point (16' east and 16' west). After co-alignment the medium and short exposures were used to replace saturated pixels in the longer expo-

tures. The combined images were corrected for instrumental vignetting and scattered X-rays. Then the pictures from the east and west off-points were aligned and joined together, and the two combined, corrected, and joined images were summed, yielding a single wide-angle exposure of nearly 121 s. The images with an original resolution of $4''906$ (half-resolution mode) have been rebinned to 4×4 macropixels, i.e., with a linear size of about $20''$. Macropixels with low counts ($\text{DN} \lesssim 100$ counts) or with strong time variability were discarded (set to zero in the images; e.g., see Fig. 4) for computation of filter ratios.

The summed images have a maximum brightness of 977,198 DN in Al.1 and 563,848 DN in Al/Mg/Mn. Given the conversion factor of detected photons n into data numbers DN, $n = (\text{DN} - 11.5)(4.23/T_{\text{MK}})$ (Tsuneta et al. 1991), which is about of order unity ($n \approx \text{DN}$) for large counts, we estimate a signal-to-noise ratio of $n^{1/2} \approx 1000$ in Al.1 and $n^{1/2} \approx 700$ in Al/Mg/Mn. In the outer corona, at a threshold of $n \gtrsim 100$ DN, the signal-to-noise ratio is still $n^{1/2} \gtrsim 10$ in each wavelength flux.

3.2. Heliographic Sector

Because our model describes the height dependence of the electron density, we subdivide the map into radial sectors (see Fig. 4), from which we sample the soft X-ray fluxes in the two filters (1, 2) as function of height, $F_1(h)$ and $F_2(h)$, averaged over areas that correspond to steps of $\Delta h = 0.02 r_\odot = 13.9 \text{ Mm} = 10''$ in height and $\Delta P = 10^\circ$ in position angle. This yields 36×2 height profiles, with height ranges varying from $0.0 < h < 0.1 r_\odot$ (at $P = 280^\circ\text{--}290^\circ$) to $0.0 < h < 0.8 r_\odot$ (at $P = 220^\circ\text{--}230^\circ$).

The sectors can be grouped into four physically distinct categories: (1) active regions, (2) coronal streamers, (3) coronal holes, and (4) quiet-Sun regions, which are

described separately in §§ 5.1–5.3. The 36 sectors are shown in Figure 4, overlaid on the Al.1 map. Two sectors are dominated by active regions, one at the east limb ($P = 180^\circ\text{--}190^\circ$) and one at the west limb ($P = 10^\circ\text{--}20^\circ$). Three sectors in the southeast are dominated by a coronal streamer ($P = 210^\circ\text{--}240^\circ$). Coronal holes affect sectors in the north ($P = 60^\circ\text{--}100^\circ$) and in the south ($P = 260^\circ\text{--}290^\circ$). One sector at the solar south pole contains no counts above our threshold ($P = 270^\circ\text{--}280^\circ$). The remaining sectors can be associated with quiet-Sun regions.

3.3. Model Fitting

Our model yields a numerical function for both filters, $F_1(h)$ and $F_2(h)$ (eq. [10]), that can be fitted in each radial sector. The model of each radial sector is constrained by four independent parameters, the electron temperature T_0 , the Gaussian temperature width σ_{T0} , the total electron density $n_0 = n_e(h_0)$ [all defined at the coronal base ($h_0 = 0$)], and the scale height factor $q_\lambda = \lambda_n/\lambda_T$. Although we have four independent parameters, we need to optimize only three parameters because one of them (n_0) is a separable scale factor. This scaling factor can be directly determined from the mean ratio of the model flux F^{model} to the observed flux F^{obs} , since $n_0 \propto (\text{EM})^{1/2} \propto F^{1/2}$,

$$n_0 = n_0^{\text{model}} \sqrt{\frac{\langle F_1^{\text{obs}}(h) \rangle}{\langle F_1^{\text{model}}(h) \rangle}}. \quad (16)$$

Thus, our model-fitting procedure essentially consists in optimizing three free parameters (T_0 , σ_{T0} , q_λ) until a minimum of a goodness criterion between the model and the observations is obtained. What goodness-of-fit criterion should we use? The method of least-squares fitting is not suitable because the fluxes vary over a range of up to 3 orders of magnitude from the inner to the outer corona, so

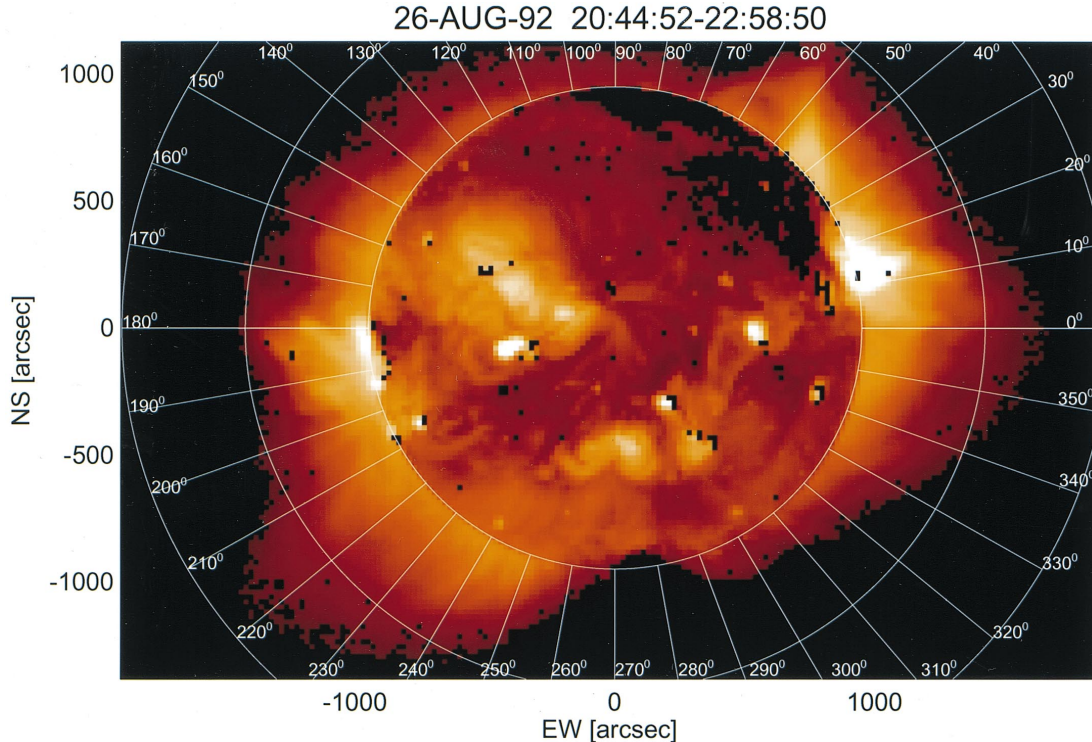


FIG. 4.—Al.1 map from *Yohkoh*/SXT with subdivision into 36 radial sectors, each $\Delta P = 10^\circ$ wide. The circles indicate altitude levels of $h = 0.0, 0.5$, and $1.0 r_\odot$. Note two active regions at the east and west, a coronal streamer in the southeast, and coronal holes in the north and south.

that a best fit would give excessive weight to the innermost corona, where the model is least accurate (because our coronal model is expected to break down in the transition region). In addition, a χ^2 fit is not reasonable because the estimated uncertainty in the counts, $\sigma_F(h) \propto [F(h)]^{1/2}$, would again give excessive weight to the innermost corona. Since we are only interested in a good overall fit over the entire coronal altitude range, we minimize the differences of the logarithmic flux in both filters,

$$\Delta F_i = \frac{1}{n} \sum_{j=1}^n |^{10} \log F^{\text{obs}}(h_j) - ^{10} \log F^{\text{model}}(h_j)|, \quad (17)$$

where n is the number of height bins and $i = 1, 2$ the two filters.

In addition, the peak temperatures T_{EM} of the DEM distributions $d\text{EM}(h, T = T_{\text{EM}})/dT$ should coincide with the filter ratio temperature $T_{\text{FR}}(h)$ obtained from the two filter fluxes because the latter corresponds to an EM-weighted temperature. An EM-weighted temperature coincides with the peak temperature for a symmetric distribution of $d\text{EM}(T)/dT$, as is the case in our model [since a Gaussian electron density distribution $dn_e(T)/dT$ implies also a Gaussian DEM distribution $d\text{EM}(T)/dT$]. We can therefore use this consistency requirement as an additional constraint in our fitting procedure. To avoid any constraints of the fit on a possible temperature gradient with height (as the data might contain), opposed to our model with isothermal field lines, we constrain only the average of the temperature,

$$\Delta T = |^{10} \log \langle T_{\text{FR}}(h) \rangle - ^{10} \log \langle T_{\text{EM}}(h) \rangle|. \quad (18)$$

For the optimization of parameters we combine the three goodness-of-fit criteria (eqs. [17] and [18]),

$$\Delta_{\text{fit}} = \Delta F_1 + \Delta F_2 + \Delta T. \quad (19)$$

We find that the best fit is always limited by the flux fit criteria (eq. [17]) because the filter ratio temperature constraint (eq. [18]) could always be satisfied ($\Delta T = 0$) in our four-parameter solutions.

Exploring the surface of the three-dimensional minimization space $\Delta_{\text{fit}}(T_0, \sigma_T, q_\lambda)$, we find that the minimum zone often contains numerous local minima of almost equal value. We tested several minimization algorithms (e.g., downhill simplex, amoeba, and Powell algorithms; see Press et al. 1986; finally we used a modified χ^2 gradient minimization algorithm that has been developed for forward-fitting of HESSI images; see M. J. Aschwanden et al. 2001, in preparation). We found that each algorithm converged to different local minima depending on the choice of initial start values. The minimum area, however, is restricted to a relatively small subspace of the entire parameter space. Therefore, we repeat each fit with randomly chosen initial parameters and accept only fits that converge to a reasonably good solution. We require in our acceptance criterion that the mean deviation is less than 10% of the observed flux, i.e., $\Delta_{\text{fit}} \leq ^{10} \log(1.1) = 0.04$. We repeat the fits as many times until we find five good solutions (within the acceptance criterion of $\Delta_{\text{fit}} \leq 0.04$) and calculate the uncertainties of the fitting parameters (T_0, σ_T, q_λ) from the mean and standard deviation ($\sigma_{T_0}, \sigma_{\sigma_{T_0}}, \sigma_{q_{\lambda 0}}$) of the five good solutions.

4. RESULTS

The results of the 36 sets of fitted data are shown in Figure 5 and in Table 1. The observed fluxes $F_1(h)$ (Al1

filter) and $F_2(h)$ (Al/Mn/Mg) are shown (Fig. 5, *histograms*) along with the best fits (Fig. 5, *thick lines*). The model fitting is applied in the largest contiguous height intervals (h_1, h_2) (Table 1, col. [3]) that exhibit a near-exponential shape (apparent as a straight line in the lin-log representation in Fig. 5). Features that deviate from a quasi-exponential function cannot be fitted by our minimal model (with four free parameters) but would require a more complex model with multiple components (§ 2.5). Nevertheless, we attempted four-parameter fits in all of the 35 radial sections with nonzero counts, in order to explore the differences between quiet-Sun regions, coronal holes, active regions, and coronal streamer regions. In the following we describe the physical parameters that have been retrieved from the best fits.

4.1. Electron Density

The best-fit values of the electron density at the coronal base, $n_0 = n_e(h = 0)$, are shown in Figure 6 (*top panel*) and listed in column (4) of Table 1. The smallest values are measured in coronal hole regions, of order $n_0 \approx (0.8\text{--}1.1) \times 10^8 \text{ cm}^{-3}$, in the northern coronal hole region around $P = 70^\circ\text{--}110^\circ$ and in the southern coronal hole region around $P = 270^\circ\text{--}300^\circ$. In quiet-Sun regions we find densities of order $n_0 \approx (1\text{--}4) \times 10^8 \text{ cm}^{-3}$, in the sectors of $P \approx 110^\circ\text{--}160^\circ$ and $P \approx 300^\circ\text{--}360^\circ$, and similarly in the coronal streamer ($P \approx 210^\circ\text{--}240^\circ$). The highest densities are found in active regions, as expected, in the order of $n_0 \approx (0.4\text{--}2.0) \times 10^9 \text{ cm}^{-3}$ (eastern active region at $P \approx 160^\circ\text{--}210^\circ$ and western active region at $P \approx 0^\circ\text{--}60^\circ$).

The height dependence of the electron density will be discussed in more detail in § 5. In most of the 36 locations the electron density drops exponentially with a scale height close to the temperature scale height, as expected for plasma in hydrostatic equilibrium. The strongest deviation from hydrostatic equilibrium is found in the coronal streamer, where the effective density scale height was found to be about twice the temperature scale height (see scale height factor q_λ in Fig. 6, *bottom panel*), and thus made the coronal plasma detectable out to a largest height of $h \approx 0.8 r_\odot$. Because the obtained scale height is contingent on the homogeneity assumption of our model, we expect some systematic error in the case of localized streamers (which could be improved by applying a two-component model as outlined in Fig. 2, *bottom panel*).

A few clarifications need to be mentioned for these density measurements. First of all, the obtained electron densities are properly accounting for line-of-sight integration and the full temperature range (within the approximations made in our model) and thus should represent far more reliable values than those generally estimated in soft X-rays based on some ad hoc assumptions on the unknown column depth. Second, these densities are defined in terms of unity filling factors but would represent lower limits in the case of lower filling factors. Third, our definition of the soft X-ray emission measure assumes an equal ion and electron density and no deviations from ionization equilibrium or abundance variations. Fourth, our model assumes quasi-isothermal plasma along each magnetic field line, an assumption that may be appropriate for the corona but certainly breaks down in the transition region and below. An effective density value should therefore be scaled to a reference height above the transition region, using the function given in equation (7). Fifth, our model assumes a

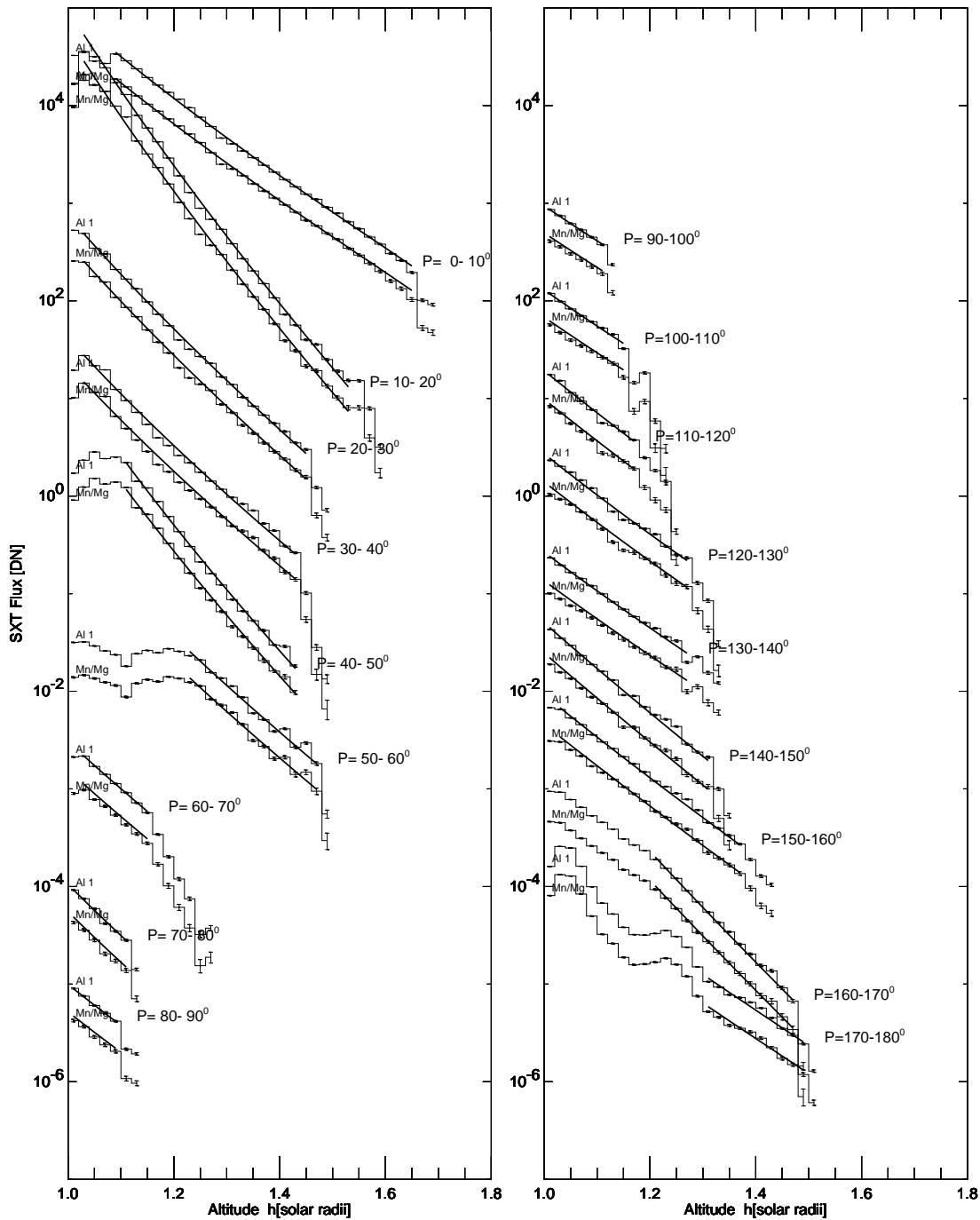


FIG. 5.—Observed radial flux profiles $F_1(h)$ and $F_2(h)$ of the Al.1 and Al/Mn/Mg filters (histograms), averaged over the indicated positions angles in the 36 sectors shown in Fig. 4, along with the best fits of our four-parameter model (thick lines). Only altitude ranges with near-exponential profiles (appearing as straight lines in the lin-log representation here) can be fitted with the single-component model. The vertical axis is offset for each profile pair by a factor of 10 for clarity.

homogeneous corona, which is probably only justified in some quiet-Sun regions and coronal holes. In inhomogeneous regions, our density measurements have to be considered as a spatial average.

4.2. Differential Emission Measure

The inferred DEM distributions $dEM(T, h = 0)/dT$ are displayed in Figure 7 (top panel) for all 36 sectors. The peak emission measure is found to have values in the range of $dEM(T = T_{EM}, h = 0)/dT \approx 10^{20}-10^{22} \text{ cm}^{-5} \text{ K}^{-1}$, with

peak temperatures in the range of $T_{EM}(h = 0) \approx 2-3 \text{ MK}$. This is compatible with differential measure distributions measured by other instruments, e.g., with SERTS (Brosius et al. 1996), where peak emission measures of $dEM(T = T_{EM}, h = 0)/dT \approx 10^{21} \text{ cm}^{-5} \text{ K}^{-1}$ at peak temperatures of $\approx 2 \text{ MK}$ were found for quiet-Sun regions and of $dEM(T = T_{EM}, h = 0)/dT \approx 2 \times 10^{21} \text{ cm}^{-5} \text{ K}^{-1}$ at $\approx 4 \text{ MK}$ in active regions (Fig. 7, bottom panel). However, note that the SERTS measurements have been performed on the disk, where the coronal emission measure is smaller than at the

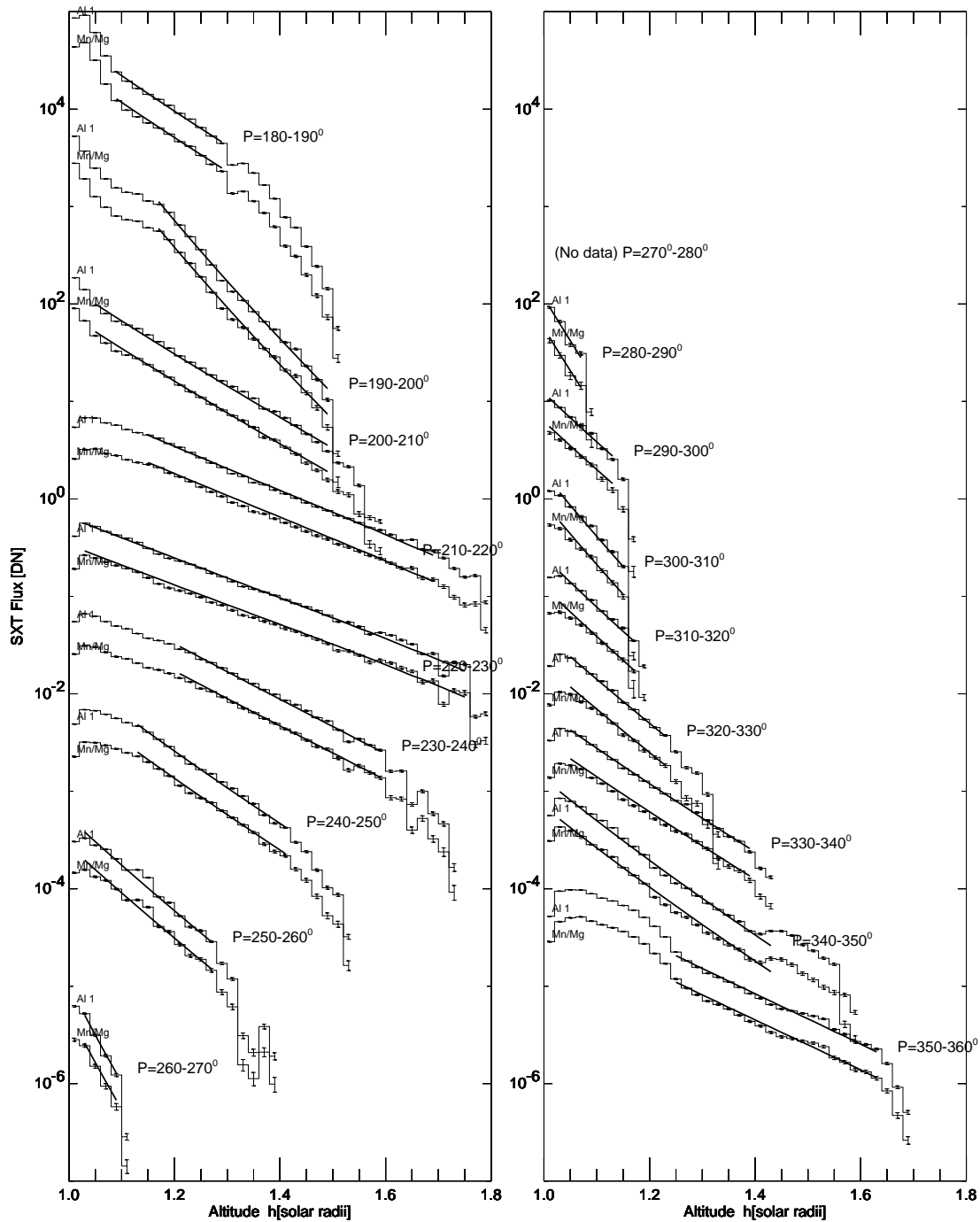


FIG. 5.—Continued

limb (as observed here) as a result of the smaller column depth along the line of sight (Fig. 3).

One property that our model is able to account for is the height dependence of the DEM distribution. For instance, the change of the DEM distribution with height is shown for sector 23 (midpoint of coronal streamer) in Figure 7 (*middle panel*). The electron temperature (at the coronal base $h = 0$) was found to be $T_0 = 1.70 \pm 0.19$ MK (see Table 1). We determine the DEM peak temperature by a parabolic fit near the maximum. We see that the distribution $dEM(T)/dT$ has a peak at $T_{EM} = 1.77$ MK at the coronal base but increases systematically to $T_{EM} = 2.76$ MK at a height of $h = 550$ Mm (Fig. 7, *middle panel*). The tem-

perature increase dT_{EM}/dh is steepest in the lowest heights and tails off asymptotically at larger heights.

The average peak temperature $\langle T_{EM}(h) \rangle$ of the emission measure distribution, averaged over the fitted height range, is shown in Figure 6 (*second panel*). This temperature is identical to the mean filter ratio temperature $\langle T_{FR}(h) \rangle$ because the filter ratio temperature is an EM-weighted temperature and coincides with the DEM peak value for symmetric distributions (as it is the case in our model by definition, based on the Gaussian differential electron density distributions). We see that the mean DEM peak temperature (or filter ratio temperature) fluctuates around $\langle T_{EM}(h) \rangle \approx 2.0$ MK for most of the quiet-Sun regions but

TABLE 1
PHYSICAL PARAMETERS OF MODEL FITTING^a TO *Yohkoh*/SXT QUIET-SUN DATA OF 1992 AUGUST 26

Sector (1)	Position Angle Range P (2)	Height Range (h_1, h_2) (3)	Electron Density n_0 (cm^{-3}) (4)	Electron Temperature T_0 (MK) (5)	Temperature Width σ_{T0} (MK) (6)	DEM Peak Temperature $\langle T_{\text{EM}}(h) \rangle$ (MK) (7)	Scale Height Ratio q_1 (8)	Fitting Deviation $\Delta \log (F)$ (9)
1	0°– 10°	1.08–1.66	$10.2 \pm 0.7 \times 10^8$	0.82 ± 0.18	1.85 ± 0.07	3.06 ± 0.42	0.93 ± 0.01	0.015
2	10°– 20°	1.02–1.54	$19.6 \pm 5.2 \times 10^8$	2.42 ± 0.47	1.01 ± 0.28	3.22 ± 0.30	0.51 ± 0.01	0.025
3	20°– 30°	1.02–1.45	$10.1 \pm 1.6 \times 10^8$	1.16 ± 0.30	1.38 ± 0.14	2.53 ± 0.37	0.79 ± 0.02	0.020
4	30°– 40°	1.02–1.43	$5.6 \pm 0.9 \times 10^8$	1.53 ± 0.34	1.43 ± 0.19	2.77 ± 0.36	0.77 ± 0.01	0.033
5	40°– 50°	1.10–1.43	$13.1 \pm 2.9 \times 10^8$	1.46 ± 0.41	1.27 ± 0.20	2.86 ± 0.26	0.60 ± 0.01	0.027
6	50°– 60°	1.22–1.47	$7.8 \pm 1.6 \times 10^8$	1.11 ± 0.34	1.37 ± 0.14	2.74 ± 0.15	0.87 ± 0.02	0.037
7	60°– 70°	1.02–1.16	$2.0 \pm 0.2 \times 10^8$	1.28 ± 0.20	1.10 ± 0.22	1.84 ± 0.14	1.10 ± 0.13	0.007
8	70°– 80°	1.01–1.12	$1.1 \pm 0.1 \times 10^8$	1.25 ± 0.24	1.42 ± 0.25	1.98 ± 0.21	0.88 ± 0.08	0.013
9	80°– 90°	1.01–1.10	$0.9 \pm 0.1 \times 10^8$	1.30 ± 0.19	1.46 ± 0.20	1.95 ± 0.17	1.03 ± 0.06	0.003
10	90°–100°	1.01–1.12	$0.8 \pm 0.1 \times 10^8$	1.49 ± 0.11	1.26 ± 0.41	1.97 ± 0.14	1.20 ± 0.06	0.004
11	100°–110°	1.01–1.16	$0.9 \pm 0.1 \times 10^8$	1.48 ± 0.13	1.41 ± 0.11	2.11 ± 0.18	1.19 ± 0.09	0.015
12	110°–120°	1.01–1.18	$1.3 \pm 0.2 \times 10^8$	1.46 ± 0.39	1.18 ± 0.34	2.02 ± 0.18	1.06 ± 0.12	0.023
13	120°–130°	1.01–1.28	$1.9 \pm 0.1 \times 10^8$	1.20 ± 0.15	1.28 ± 0.11	2.05 ± 0.26	1.09 ± 0.04	0.030
14	130°–140°	1.01–1.28	$1.8 \pm 0.1 \times 10^8$	1.32 ± 0.07	1.14 ± 0.06	1.97 ± 0.21	1.26 ± 0.02	0.031
15	140°–150°	1.01–1.32	$2.9 \pm 0.4 \times 10^8$	1.32 ± 0.28	0.92 ± 0.23	1.87 ± 0.20	1.16 ± 0.07	0.029
16	150°–160°	1.02–1.38	$3.5 \pm 0.4 \times 10^8$	1.27 ± 0.27	1.08 ± 0.20	2.03 ± 0.22	1.21 ± 0.05	0.021
17	160°–170°	1.20–1.48	$10.8 \pm 4.0 \times 10^8$	1.23 ± 0.41	0.83 ± 0.18	2.12 ± 0.11	0.93 ± 0.02	0.016
18	170°–180°	1.30–1.50	$5.7 \pm 1.4 \times 10^8$	1.44 ± 0.23	0.79 ± 0.12	2.10 ± 0.06	1.38 ± 0.06	0.027
19	180°–190°	1.08–1.30	$6.8 \pm 1.6 \times 10^8$	1.36 ± 0.56	1.37 ± 0.37	2.35 ± 0.16	1.15 ± 0.07	0.021
20	190°–200°	1.16–1.50	$18.7 \pm 3.9 \times 10^8$	1.12 ± 0.34	1.22 ± 0.14	2.67 ± 0.21	0.70 ± 0.00	0.032
21	200°–210°	1.04–1.50	$3.9 \pm 0.1 \times 10^8$	1.32 ± 0.09	1.21 ± 0.06	2.24 ± 0.24	1.38 ± 0.03	0.023
22	210°–220°	1.15–1.70	$2.9 \pm 0.3 \times 10^8$	1.31 ± 0.22	1.26 ± 0.15	2.31 ± 0.19	2.01 ± 0.05	0.020
23	220°–230°	1.02–1.76	$1.7 \pm 0.1 \times 10^8$	1.70 ± 0.19	1.10 ± 0.18	2.30 ± 0.20	2.30 ± 0.08	0.028
24	230°–240°	1.20–1.60	$4.3 \pm 0.2 \times 10^8$	0.85 ± 0.17	1.45 ± 0.11	2.36 ± 0.18	1.61 ± 0.04	0.018
25	240°–250°	1.12–1.42	$4.5 \pm 1.2 \times 10^8$	1.22 ± 0.39	1.21 ± 0.19	2.27 ± 0.16	1.22 ± 0.06	0.020
26	250°–260°	1.02–1.28	$2.5 \pm 0.6 \times 10^8$	1.32 ± 0.51	1.18 ± 0.33	2.12 ± 0.22	0.99 ± 0.05	0.036
27	260°–270°	1.02–1.10	$1.9 \pm 0.2 \times 10^8$	1.00 ± 0.20	1.17 ± 0.16	1.86 ± 0.17	0.49 ± 0.00	0.026
29	280°–290°	1.01–1.08	$0.8 \pm 0.1 \times 10^8$	1.58 ± 0.12	0.76 ± 0.22	1.79 ± 0.08	0.72 ± 0.06	0.030
30	290°–300°	1.00–1.13	$1.1 \pm 0.1 \times 10^8$	1.64 ± 0.17	0.81 ± 0.23	1.88 ± 0.09	1.12 ± 0.20	0.028
31	300°–310°	1.02–1.16	$1.8 \pm 0.2 \times 10^8$	1.28 ± 0.16	1.03 ± 0.12	1.88 ± 0.15	0.82 ± 0.03	0.026
32	310°–320°	1.02–1.18	$2.2 \pm 0.4 \times 10^8$	1.14 ± 0.31	1.07 ± 0.25	1.76 ± 0.15	1.10 ± 0.13	0.026
33	320°–330°	1.04–1.24	$3.0 \pm 0.6 \times 10^8$	1.20 ± 0.30	0.96 ± 0.22	1.80 ± 0.14	1.16 ± 0.10	0.027
34	330°–340°	1.04–1.40	$3.3 \pm 0.6 \times 10^8$	1.14 ± 0.33	1.12 ± 0.20	1.99 ± 0.21	1.35 ± 0.05	0.021
35	340°–350°	1.02–1.44	$3.5 \pm 0.8 \times 10^8$	1.47 ± 0.47	1.09 ± 0.35	2.22 ± 0.23	1.17 ± 0.07	0.034
36	350°–360°	1.24–1.64	$2.8 \pm 0.4 \times 10^8$	1.22 ± 0.27	1.42 ± 0.14	2.53 ± 0.15	1.69 ± 0.09	0.025

^a The quoted uncertainties represent the standard deviations from repeated forward-fitting of the model (see § 3.3).

increases to ≈ 2.5 – 3.5 MK in active regions (Fig. 6, *second panel*). The mean DEM peak temperatures, $\langle T_{\text{EM}}(h) \rangle$, averaged over the fitted height ranges (h_1, h_2), are also listed in column (7) of Table 1.

4.3. Electron Temperature

In our model we defined a differential electron density distribution $dn_e(T)/dT$ (eq. [1]), which has a peak at T_0 at a reference height of $h_0 = 0$. We show the best-fit values of these electron temperatures T_0 (defined at height $h_0 = 0$) in Figure 6 (*second panel*) and in Table 1 (col. [5]). These electron temperatures vary around $T_0 \approx 1.0$ – 1.5 MK for most of the analyzed regions. A significantly higher value is only observed in the western active region at $P = 10^\circ$ – 20° , with a value of $T_0 \approx 2.4$ MK. The temperature spread is generally of the same order, $\sigma_{T0} \approx T_0 \approx 1.0$ – 1.5 MK (Fig. 6, *third panel*; Table 1, col. [6]). Therefore, the effective distributions of electron temperatures, $(T_0 - \sigma_{T0}, T_0 + \sigma_{T0})$, cover a full range from $\approx (0.5, 2.0)$ to $(0.5, 3.0)$ MK in most locations on the Sun. (No statement can be made for temperatures below $\lesssim 0.5$ MK because of the insensitivity of

Yohkoh/SXT and our single-Gaussian approximation of the DEM distribution.)

The peak temperature T_{EM} in the DEM distribution as discussed in the previous section represents a convolved quantity, i.e., an EM-weighted line-of-sight average over many different temperatures. In hydrostatic atmospheres, such an EM-weighted average yields a variation of the mean temperature $T_{\text{EM}}(h)$ with height because higher temperatures have larger scale heights. The comparison of the electron temperature T_0 at the coronal base ($h_0 = 0$) with the DEM peak temperature $\langle T_{\text{EM}}(h) \rangle$ averaged over the fitted height range (Fig. 6, *second panel*) clearly demonstrates a systematic increase of the DEM temperature with height. This bias merely reflects the linear dependence of the density scale heights λ_T with temperature T (eq. [5]), which gives the higher temperatures relatively more weight at larger heights, when an EM-weighted temperature $T_{\text{EM}}(h)$ is determined. If the DEM distribution is symmetric, the peak temperature $T_{\text{EM}}(h)$ coincides with the mean electron temperature $T_e(h)$, i.e., $T_{\text{EM}}(h = h_0) = T_0$ at the coronal base $h_0 = 0$. The comparison in Figure 6 (*second panel*) illus-

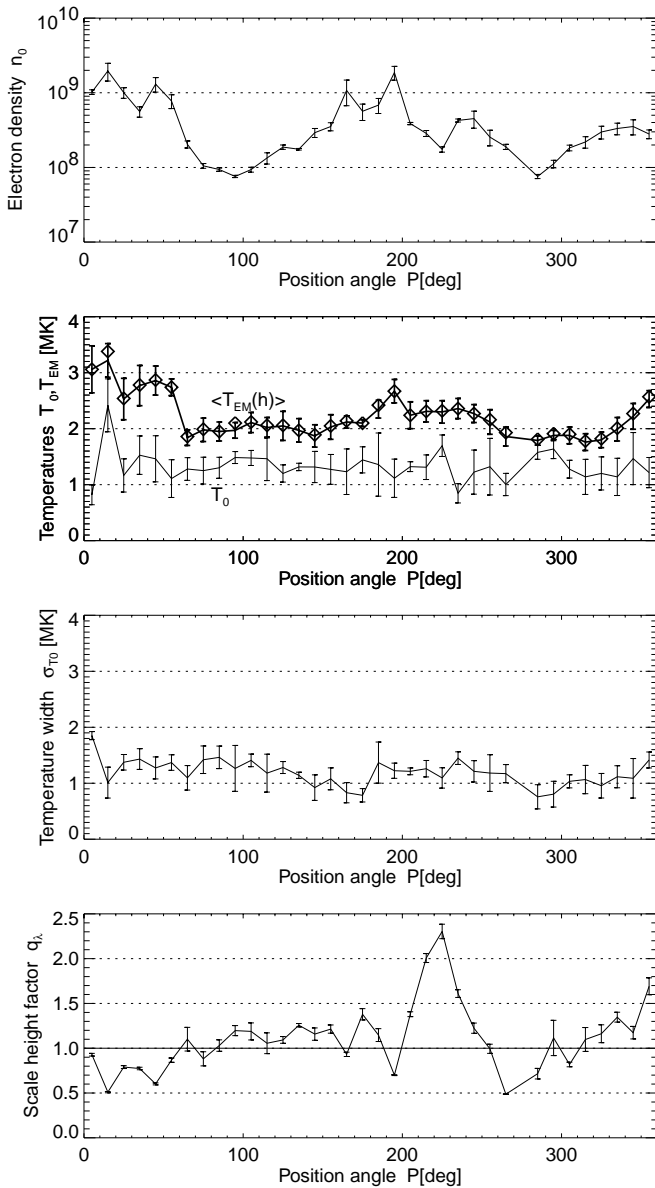


FIG. 6.—Best-fit parameters as a function of the position angle P (see also Table 1): the base electron density n_0 (top panel), the electron temperature T_0 and DEM peak temperature $\langle T_{EM}(h) \rangle$ (second panel), the (Gaussian) temperature width σ_{T_0} (third panel), and the scale height factor q_s (bottom panel). The DEM peak temperature is given at the coronal base (T_0), averaged over the fitted height range ($\langle T(h) \rangle$) and the average filter ratio temperature ($\langle T_{FR}(h) \rangle$; diamonds). The error bars indicate the standard deviation of five best-fit solutions.

rates that the DEM-weighted temperature, averaged over the fitted height ranges, is systematically about 50% higher than the electron temperature T_0 at the coronal base ($h_0 = 0$).

4.4. Temperature Gradients

We turn now to the variation of the temperature with height, $T(h)$. Our model is based on the simplest assumption that is compatible with observations, i.e., near-isothermal flux tubes. However, the temperature spread of the differential electron density $dn_e(T)/dT$ and the related DEM distribution $dEM(T)/dT$ is expected to lead to a systematic temperature increase with height h for any EM-weighted temperature measurement, such as the filter ratio method.

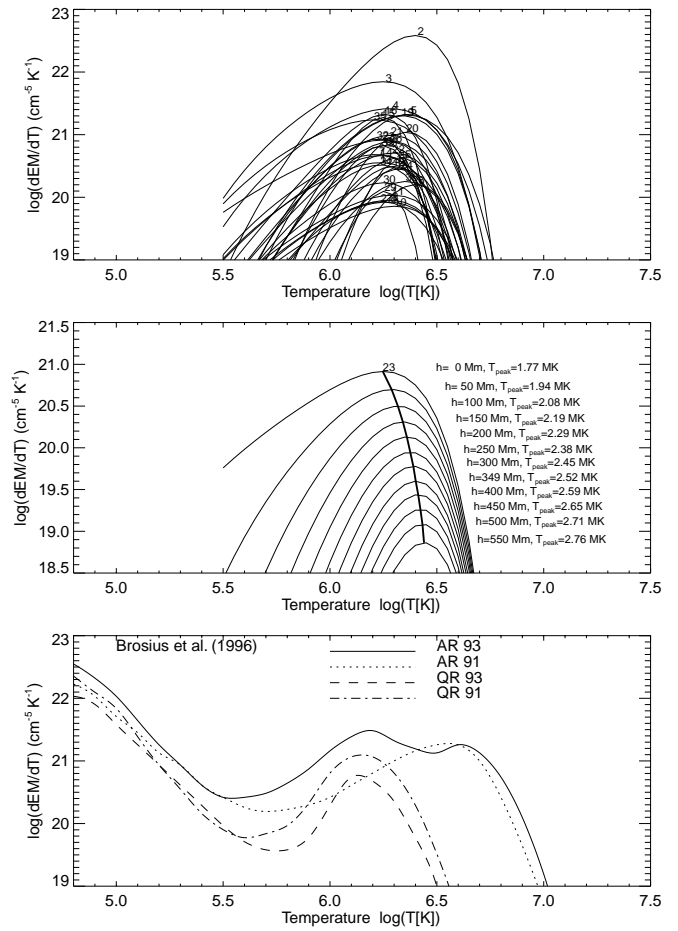


FIG. 7.—Model-inferred DEM distributions $dEM(T, h = 0)/dT$, numbered by the sectors 1–36 (top panel). The height dependence of one DEM curve is shown for sector 23, which coincides with the midpoint of a coronal streamer (middle panel). Note the systematic increase of the peak temperature from $T_{EM} = 1.77$ MK at the coronal base ($h = 0$) to $T_{EM} = 2.76$ MK at a height of $h = 550$ Mm. For comparison, four DEM curves from Brosius et al. (1996) are shown, derived from iron lines observed with SERTS (bottom panel).

We show the height dependence of the emission measure peak temperature graphically in Figure 8 (top panel) and in quantitative numbers in Figure 9 (solid lines). In both figures we show also the effectively measured filter ratio temperatures (Fig. 8, bottom panel; Fig. 9, crosses). In many sectors we find remarkably good agreement between the DEM temperature gradient $dT_{EM}(h)/dh$ and the filter ratio temperature gradient $dT_{FR}(h)/dh$. From the 36 panels in Figure 9 we find the best agreement for the following sectors: $P = 60^\circ$ – 160° and $P = 210^\circ$ – 340° . These two ranges include primarily quiet-Sun regions, coronal holes, and coronal streamers. Only in areas of active regions ($P = 0^\circ$ – 60° , 160° – 210° , 330° – 360°) do we find disagreement, which is probably related to the inadequacy of our single-component model for the more complex and inhomogeneously structured active regions. Nevertheless, the agreement in the more homogeneously structured regions reveals that the effect of broadband emission measure distributions combined with the theoretical assumption of hydrostatic equilibrium accurately predicts the apparent temperature increase of filter ratio temperatures with height, $dT_{EM}(h)/dh$, an effect that was recently pointed out by Aschwanden & Nitta (2000). We emphasize that this appar-

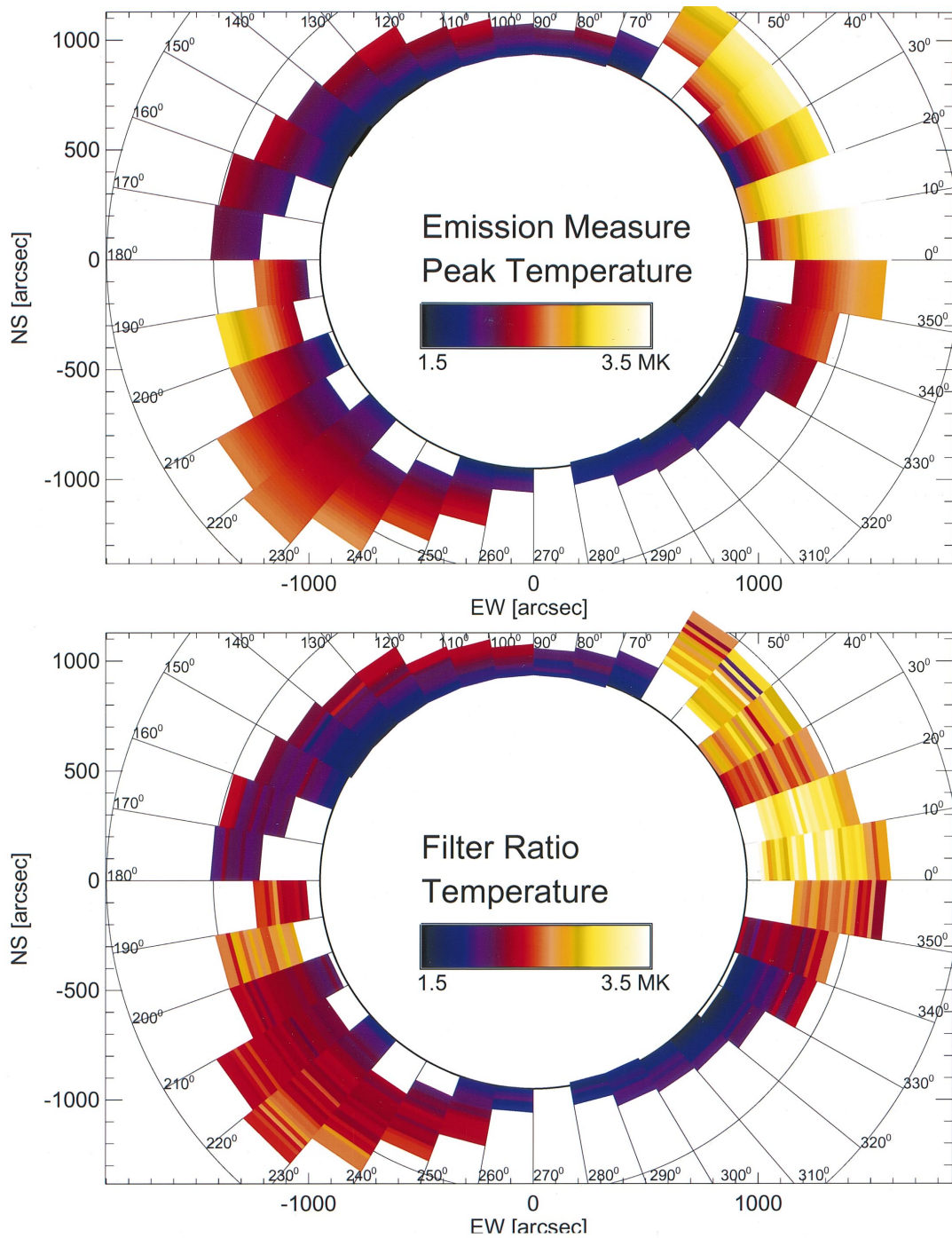


FIG. 8.—Coronal temperature maps derived in the fitted height ranges of 36 sectors, either from the DEM peak temperature $T_{\text{EM}}(h)$ (top panel) or with the standard filter ratio temperature method (bottom panel). Note that their values averaged over the fitted height ranges could be constrained to be identical within the degrees of freedom of our four-parameter model.

ent temperature gradient does *not* mean that the intrinsic electron temperature increases with height along a single field line. In our model we assumed that each field line is isothermal in itself, an assumption that we find to be fully consistent with the (DEM-weighted) filter ratio temperature with height.

4.5. Scale Heights

We show the best-fit values of the scale height factors $q_\lambda = \lambda_p/\lambda_T$ in Figure 6 (bottom panel). We find that these

scale height factors are of order unity in about half of the measured locations, say within $q_\lambda = 1.0 \pm 0.2$, in particular in quiet-Sun regions and in coronal holes ($P = 60^\circ\text{--}190^\circ$, $P = 290^\circ\text{--}330^\circ$). We can therefore conclude that flux tubes in quiet-Sun regions and coronal holes are close to hydrostatic equilibrium.

The biggest deviation from hydrostatic equilibrium is found in the region of the coronal streamer ($P = 200^\circ\text{--}250^\circ$), reaching values of $q_\lambda \approx 2$. This could be explained with the dynamic nature of coronal streamers, which have

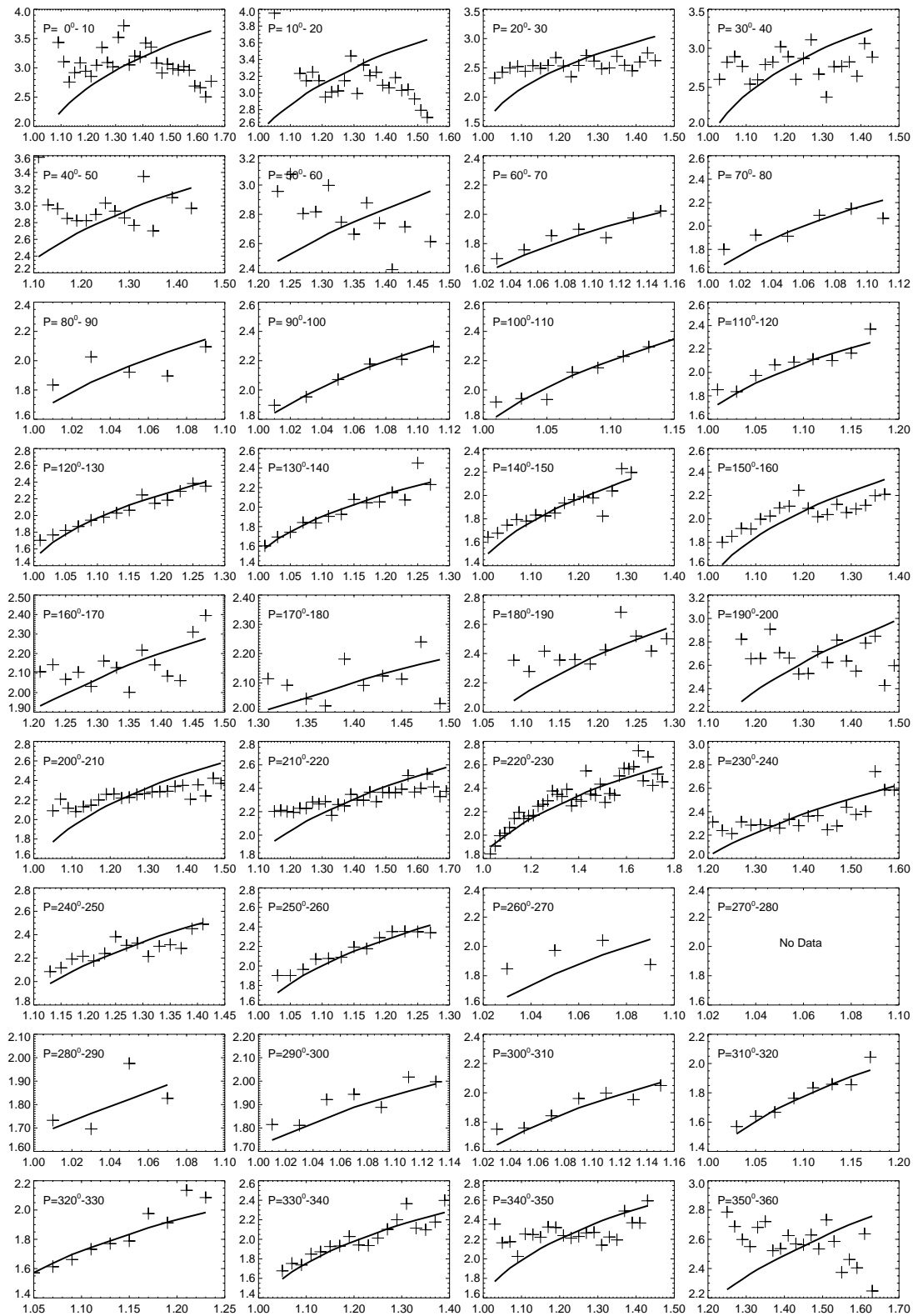


FIG. 9.—Functional dependence of the DEM peak temperature $T_{EM}(h)$ vs. height h (thick solid curve) and corresponding standard filter ratio temperature $T_{FR}(h)$ (crosses), averaged over the same position angle ranges as shown in Fig. 8. Note the detailed agreement in quiet-Sun regions, coronal hole regions, and the coronal streamer region.

mass flows that deviate from hydrostatic equilibrium by definition. Although the measurement of scale heights in streamers is probably less accurate than in quiet-Sun regions because of the homogeneity assumption of our model, the result of superhydrostatic scale heights in

streamers is corroborated by the large height range of detectability (up to altitudes of $0.8 r_\odot$) as well as by a new result that the majority of large-scale EUV loops were found to have dynamic behavior and superhydrostatic scale heights (Aschwanden, Nightingale, & Alexander 2000).

Another deviation from hydrostatic equilibrium is found in active regions, where the ratio drops to $q_\lambda \approx 0.5$. Here we have to caution that our minimal single-component model is probably not adequate to describe the complexity of an active region, in particular in the presence of closed-loop systems. If there are more small-scale loops with higher pressures than large-scale loops, the statistical decrease of density with height is steeper than for open loops in hydrostatic equilibrium and thus could easily explain the statistically shorter scale height factors $0.5 \lesssim q_\lambda \lesssim 1.0$.

5. DISCUSSION

Our approach of forward-fitting the DEM distribution to soft X-ray fluxes yields a self-consistent density and temperature diagnostic that is largely independent of wavelengths and the detector response. To our knowledge this is the first attempt to derive the DEM distribution from soft X-rays, in particular from the *Yohkoh*/SXT. It is therefore important to compare the results of our density and temperature diagnostic with previous measurements, to verify the validity and viability of our new method.

We provide a comparison with other coronal density measurements in Figure 10, where our observed 35 density profiles $n_e(h)$ are grouped into four categories: (1) coronal holes, (2) quiet Sun, (3) coronal streamers, and (4) active regions. For compilations of coronal density measurements we consulted Habbal, Esser, & Arndt (1993) and Esser & Sasselov (1999).

5.1. Coronal Holes

Our measurements in coronal holes are restricted to a height range of $0.01 \leq h \leq 0.12 r_\odot$ ($\lesssim 85$ Mm). In the northern coronal hole ($P = 70^\circ$ – 100°) we find a mean electron density of $n_e = (0.93 \pm 0.15) \times 10^8 \text{ cm}^{-3}$, an electron temperature of $T_0 = 1.35 \pm 0.12$ MK, a temperature spread of $\sigma_{T_0} = 1.38 \pm 0.10$ MK, and a mean scale height factor of $q_\lambda = 1.03 \pm 0.16$. In the southern coronal hole ($P = 260^\circ$ – 290°) we find a mean electron density of $n_e = (1.32 \pm 0.56) \times 10^8 \text{ cm}^{-3}$, an electron temperature of $T_0 = 1.29 \pm 0.29$ MK, a temperature spread of $\sigma_{T_0} = 0.97 \pm 0.21$ MK, and a mean scale height factor of $q_\lambda = 0.60 \pm 0.11$. All these values are computed for a reference height of $h = 0$ at the coronal base. Other measurements of electron densities in coronal holes at comparable height levels have all been reported to be higher, up to an order of magnitude: $n_e = (1.7\text{--}5) \times 10^8 \text{ cm}^{-3}$ at $h = 0.03 r_\odot$ (Ahmad & Withbroe 1977; Mariska 1978); $n_e = (7\text{--}8) \times 10^8 \text{ cm}^{-3}$ at $h = 0.04 r_\odot$ (Ahmad & Webb 1978); $n_e = (0.41\text{--}2.3) \times 10^8 \text{ cm}^{-3}$ at $h = 0.1 r_\odot$ (Saito 1965; Bohlin, Sheeley, & Tousey 1975; Mariska 1978); $n_e = (0.45\text{--}0.62) \times 10^8 \text{ cm}^{-3}$ at $h = 0.15 r_\odot$ (Guhathakurta et al. 1992); $n_e = 2.0 \times 10^8 \text{ cm}^{-3}$ at $h = 0.2 r_\odot$ (van de Hulst 1950a, 1950b). However, recent measurements from Si VIII, Si IX, and S X line ratios observed with *SOHO*/SUMER are in much better agreement, which yield $n_e \approx 1.0\text{--}1.5 \times 10^8 \text{ cm}^{-3}$ in a temperature range of $T \approx 0.8\text{--}1.3$ MK at the coronal base (Doscsek et al. 1997; Guhathakurta & Fischer 1998; Guhathakurta et al. 1999). Similarly, measurements from Si XII, Mg IX, and Mg X with *SOHO*/CDS yield comparable densities of $n_e = 1.2 \times 10^8 \text{ cm}^{-3}$ in the darkest areas of coronal holes, with temperatures of $T = 0.82$ MK (Fludra et al. 1999). Although our measurements in coronal holes extend only up to a height of $h \lesssim 0.1 r_\odot$, our densities seem to be generally lower than most of the older measurements from white-light

coronagraphs. Only the white-light measurements from Lallemand, Holzer, & Munro (1986) and those from Koutchmy (1977) find lower densities in coronal holes than here. The latter were obtained during an eclipse, when stray light conditions are much better than in typical coronagraph observations, which may contaminate low electron density measurements. At heights of $h \approx 0.1 r_\odot$, coronal density measurements inferred from spectral lines seem to yield systematically lower values than white-light observations, using the polarized brightness method. The latter discrepancy between the two sets of measurements was also pointed out by Esser & Sasselov (1999), who suspect that polarized brightness might give an overestimation of the electron densities below $h \lesssim 0.5 r_\odot$. A consequence of this uncertainty is that coronal density models are ill-constrained in the transition region at heights of $0.002 \lesssim h \lesssim 0.1 r_\odot$, which is most important to model the energy input into the solar wind. The only currently existing model that interleaves chromospheric with coronal density models is due to Hansteen, Leer, & Holzer (1997), shown in an expanded view in Figure 11. Note that our new soft X-ray measurements from *Yohkoh*/SXT seem to bridge the gap between coronal white-light density measurements and the chromospheric density models (based on spectral lines measured at heights of $h \lesssim 0.004 r_\odot$) and thus provide more stringent constraints for solar wind models.

Our coronal hole temperature measurements with $T_0 \approx 1.3$ MK and $\sigma_{T_0} \approx 1.0$ MK are in rough agreement with the range of previously measured temperatures, which scatter in the range of $T_{\text{CH}} \approx 0.8\text{--}1.4$ MK (see compilation in Habbal et al. 1993 and newer measurements by Wilhelm et al. 1998; Del Zanna & Bromage 1999; Zhang, White, & Kundu 1999). Note that the DEM distribution includes the temperature contributions from all plasmas along a given line of sight. Therefore, based on our average DEM distribution of $T_0 = 1.3 \pm 1.0$ MK, the uncontaminated temperature in a coronal hole may well be as low as $T_1 \approx 0.8 \pm 0.5$ MK, if balanced by an equal amount of hotter (contaminating) plasma in the foreground or background with a distribution of $T_2 \approx 1.8 \pm 0.5$ MK. Such a coronal hole model would also be more consistent with other DEM reconstructions using multiple Mg, Si, and Fe lines measured with CDS, showing DEM peaks around $T_{\text{CH}} \approx 0.8\text{--}1.0$ MK (Fig. 5 in Del Zanna & Bromage 1999).

From these data comparisons we draw three conclusions: (1) *Yohkoh*/SXT is able to characterize the true DEM distribution down to the low-temperature limit of its response function, which borders EUV wavelengths ($T \approx 1.0\text{--}1.5$ MK), despite its main high-temperature sensitivity in the range of $T = 2\text{--}20$ MK; (2) the electron densities in coronal holes measured with soft X-rays are found to be in good agreement with EUV line ratio measurements but are about 2–10 times lower than white-light measurements obtained with the polarized brightness method (we caution that our soft X-ray measurements always represent lower limits because we assumed a filling factor of unity; the presence of a dark coronal hole on the visible solar disk in front of a brighter background from the back side of the Sun implies some overestimate on the front side and a corresponding underestimate on the back side); and (3) the SXR-inferred densities in coronal holes agree better with recent solar wind models (e.g., from Hansteen et al. 1997) than most of the white-light measurements in the height range of $0.02 < h < 0.2 r_\odot$.

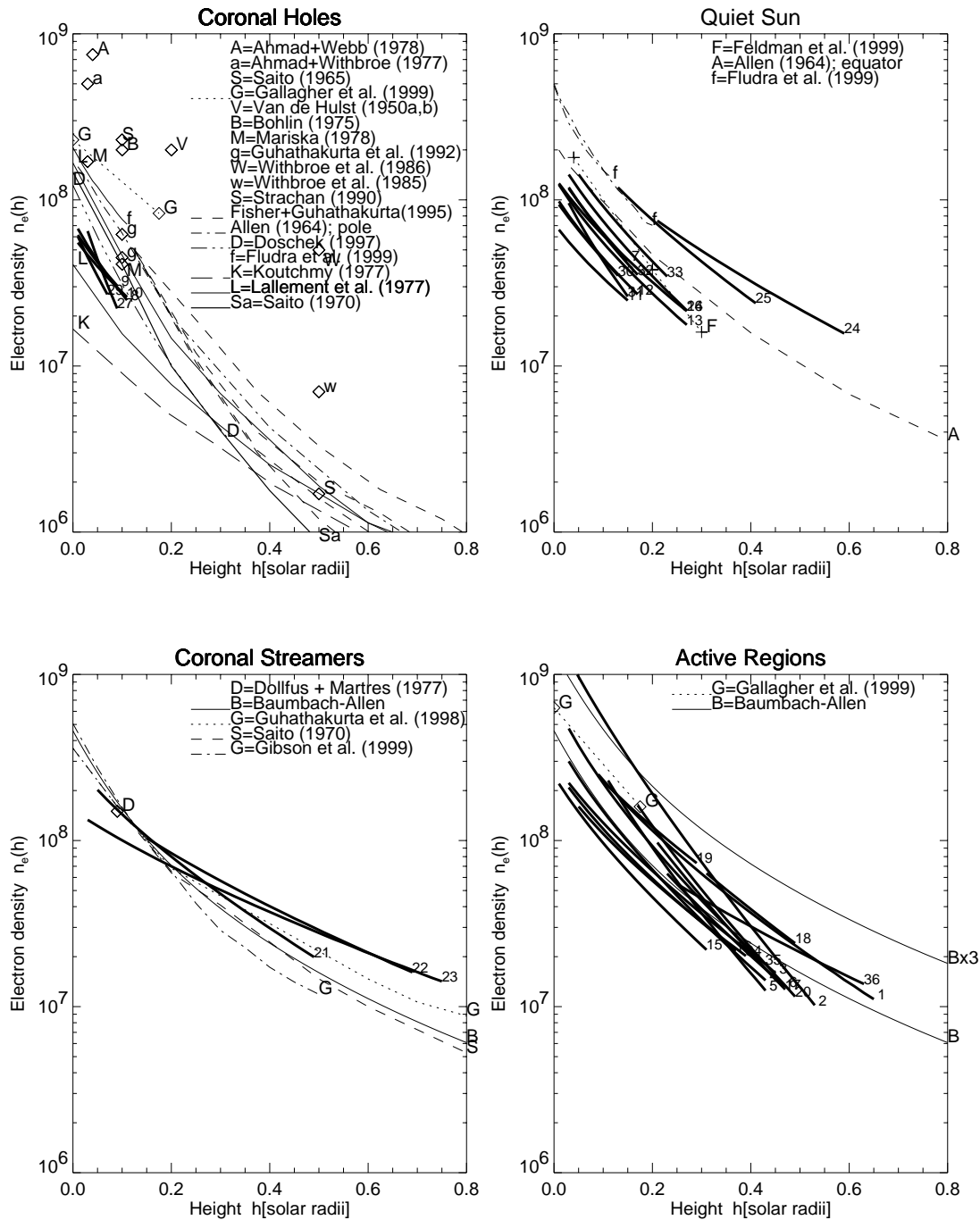


FIG. 10.—Comparison of our coronal density measurements $n_e(h)$ with previous measurements. The four diagrams contain our 35 measurements (thick lines, labeled with numbers; see Table 1). Single-height measurements by other workers are marked with diamonds and letters; multiple measurements covering some height range are rendered with different line styles. (Fisher & Guhathakurta 1995; Gallagher et al. 1999).

5.2. Quiet Sun

In contrast to coronal holes, which by definition encompass regions with open-field lines that connect with interplanetary space, the so-called quiet Sun is made up of closed-field regions, with static behavior or only slowly varying changes. Let us evaluate typical parameters from two different quiet-Sun regions, one at northeast at $P = 100^\circ$ – 140° and one at southwest at $P = 290^\circ$ – 330° . The mean electron densities there are $n_e = (2.0 \pm 0.7) \times 10^8 \text{ cm}^{-3}$ and $n_e = (1.8 \pm 0.9) \times 10^8 \text{ cm}^{-3}$ at the coronal base ($h = 0$). The corresponding mean electron temperatures are

$T_0 = 1.3 \pm 0.1 \text{ MK}$ and $T_0 = 1.4 \pm 0.2 \text{ MK}$. The scale height factors are $q_\lambda = 1.14 \pm 0.09$ and $q_\lambda = 0.98 \pm 0.20$, consistent with hydrostatic equilibrium. These values compare favorably with recent measurements using density-sensitive silicon lines from *SOHO*/SUMER, where an isothermal EM with a peak temperature of $T = 1.3 \text{ MK}$ was found, as well as a density decrease from $n_e = 1.8 \times 10^8 \text{ cm}^{-3}$ to $n_e = 0.16 \times 10^8 \text{ cm}^{-3}$ over a height range of $h = 0.04$ – $0.30 r_\odot$ [Feldman et al. 1999; see density profiles $n_e(h)$ in Fig. 10, top right panel]. Our density measurements in quiet-Sun regions are also consistent with Allen's (1964)

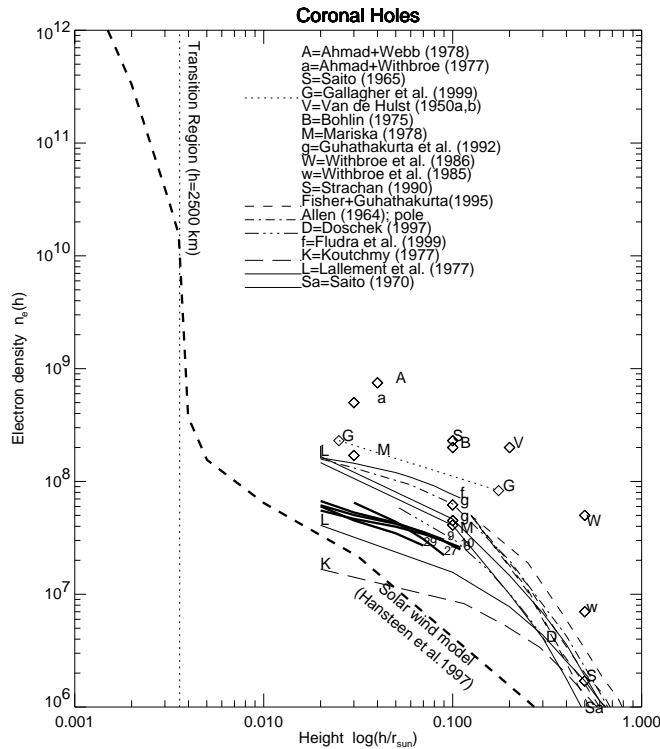


FIG. 11.—Expanded representation of coronal hole measurements on log-log scale, including a solar wind model by Hansteen et al. (1997) that interfaces chromospheric density models with solar wind models (*thick dashed line*). Because some lower limits of the heights are not exactly known ($h \approx 0$), we set a finite value of $h \gtrsim 0.02 r_{\odot}$ on this log scale, which is equal to the lowest limit of our SXT measurements (with macropixels of $20''$). Note that our SXR measurements (*thick solid lines*) bridge the white-light measurements to the solar wind model.

standard values for the equatorial corona, say within a factor of 2 (Fig. 10, *top right panel*). Recent density measurements of an equatorial region from Si ix 342/350 line ratios yield similar hydrostatic density profiles that are consistent with our highest quiet-Sun values (Fludra et al. 1999). The agreement of our soft X-ray measurements (which constitute lower limits) with diagnostic from density-sensitive spectral line pairs (e.g., Si ix 342/350) (which represent upper limits) indicates that the filling factor of the soft X-ray-emitting plasma is close to unity.

The electron density of the quiet Sun has also been determined from eight ionization states from Fe x through Fe xvii, using SERTS observations (Brosius et al. 1996). For a quiet-Sun region observed during 1993 they find a density of $\log(n_e(\text{cm}^{-3})) = 9.03 \pm 0.28$, which is about an order of magnitude higher than what we observe in soft X-rays. However, their DEM distribution includes also cooler plasma from the transition region, which, below a temperature limit of $\log(T_e) \approx 5.3$, outweighs the hotter coronal plasma by mass (see Fig. 7, *bottom panel*). The minimum in the DEM distribution, around $\log(T) \approx 5.7$ (i.e., $T \approx 0.5$ MK), which is the peak of the radiative loss function, thus approximately represents the “continental divide” between chromospheric and coronal plasma. Using a single-Gaussian function to characterize the differential electron distribution $dn_e(T)/dT$, as we are doing here (eq. [1]), therefore restricts the DEM approximation to temperatures above the DEM minimum at $T \approx 0.5$ MK and thus separates also the coronal from the chromospheric density in our model.

Thus, we conclude that (1) the quiet corona is in hydrostatic equilibrium, (2) the filling factor of soft X-ray plasma is close to unity, and (3) the coronal density includes mainly plasma with temperatures $T \gtrsim 0.5$ MK.

5.3. Coronal Streamers

Our SXR density measurements $n_e(h)$ in coronal streamers are in agreement with previous measurements from other instruments and wavelengths within a factor of $\lesssim 2$ (Fig. 10, *bottom left*), e.g., with white-light measurements (Saito 1970; Dollfus & Martres 1977; data from Guhathakurta and colleagues published in Esser & Sassellov 1999; Gibson et al. 1999). However, whether the density profile $n_e(h)$ is hydrostatic or not depends on the temperature measurements, which differ much more from ours than the density measurements.

The temperature structure of coronal streamers seems to be strongly model dependent. In our model, each field line of the coronal streamer is isothermal, with a DEM distribution of $T_0 = 1.7$ MK and $\sigma_{T_0} = 1.1$ MK at the base of the streamer (at $P = 220^\circ - 230^\circ$). The apparent temperature increase with height, up to a maximum temperature of $T(h = 0.7 r_{\odot}) \approx 2.7$ MK at a height of $h = 0.7 r_{\odot}$, is entirely an effect of scale height weighting of the broadband DEM temperature distribution. In contrast, isothermal line-of-sight models obtain quite different temperature profiles. For instance, from white-light data inverted with the van de Hulst (1950a, 1950b) method and assuming hydrostatic equilibrium along the streamer, a temperature maximum of $T \approx 1.5$ MK at a height of $h \approx 0.2 - 0.5 r_{\odot}$ was reported, while the temperature decreases at higher altitudes down to $T \approx 0.7$ MK at a height of $h \approx 3 r_{\odot}$ (Gibson et al. 1999; similar results were also obtained by Guhathakurta et al. 1999). From the same data, using a tomographic inversion, a much higher temperature was inferred for this streamer, i.e., $T = 1.9$ MK (Zidowitz 1999). The fact that white-light data with the hydrostatic assumption yielded a similar temperature ($T \approx 1.2 - 1.4$ MK) at a particular height of $h \approx 0.2 r_{\odot}$ as independently determined by CDS spectral data was interpreted as meaning that the hydrostatic equilibrium is a plausible assumption (Gibson et al. 1999). In contrast, we find here that the density scale height exceeds the hydrostatic scale height up to a factor of $q_{\lambda} = 2.3$ in the streamer and thus cannot escape the conclusion that coronal streamers are *not* in hydrostatic equilibrium. These discrepancies in temperature measurements in streamers are a consequence of different model constraints. Obviously, both the hydrostatic equilibrium assumption as well as the single-temperature assumption (along each line of sight) are two strong constraints that lead to quite different results from models where these constraints are relaxed (like in our DEM model).

5.4. The DEM Model Applied to the Baumbach-Allen Formula

The white-light spectrum of the solar corona is composed of three components: (1) the K corona, made of partially polarized continuum emission from photospheric light scattered at free electrons (dominating at $h \lesssim 0.3 r_{\odot}$); (2) the L corona, consisting of spectral line emission from highly ionized atoms (dominating at $h \lesssim 0.5 r_{\odot}$); and (3) the F corona, which presents absorption lines of the photospheric Fraunhofer spectrum caused by diffraction from interplanetary dust (dominating at $h \gtrsim 0.5 r_{\odot}$). The line-of-sight inte-

grated density profiles of these three components can be approximated by a power law each, leading to an average density profile known as the Baumbach-Allen formula,

$$n_e(R) = 10^8 \left(\frac{2.99}{R^{-1.6}} + \frac{1.55}{R^{-6}} + \frac{0.036}{R^{1.5}} \right) \text{ cm}^{-3}, \quad (20)$$

parametrized by the distance $R = 1 + h/r_\odot$ from Sun center. This density profile is shown in Figure 12 (*squares*).

We fit now each of these three components with our line-of-sight integrated DEM model. Approximate fits are shown in Figure 12. The coronal base densities n_0 are directly given by the Baumbach-Allen formula (eq. [20]), i.e., $n_0 = 2.99 \times 10^8 \text{ cm}^{-3}$ (K corona), $n_0 = 1.55 \times 10^8 \text{ cm}^{-3}$ (L corona), and $n_0 = 3.6 \times 10^6 \text{ cm}^{-3}$ (F corona), where the densities of the K and L coronae (see fits in Fig. 12) are fully consistent with other quiet-Sun values we infer here. In addition, the DEM temperature ranges inferred from the best fits, $T = 0.75\text{--}1.25 \text{ MK}$ for the K corona and $T = 0.9\text{--}2.3 \text{ MK}$ for the F and L coronae, are fully consistent with quiet-Sun values. Most interesting is that the best fits confirm that the K corona is exactly hydrostatic, i.e., $q_\lambda = 1.0$ (Fig. 12), while the L corona has an extended scale height of $q_\lambda = 1.9$ times the hydrostatic scale height, a value that is typical for coronal streamers. We can therefore associate the L corona entirely to coronal streamer regions. Finally, the F corona exhibits an extreme density scale height factor of $q_\lambda \approx 10$ times the hydrostatic scale height. Such an excessive scale height cannot be consistent with gravitational stratification. It is therefore obvious that the F corona does not represent coronal plasma in hydrostatic equilibrium but rather the density distribution of interplanetary dust that has its own dynamics escaping solar gravitation.

Thus, our DEM model not only is capable of reproducing the Baumbach-Allen formula and each of its three coronal components quantitatively in detail (see fits in Fig. 12) but also provides additional physical information that is not explicitly used in the derivation of the Baumbach-Allen formula, namely, the DEM temperature ranges and the density scale heights of the three coronal components. We can therefore relate the six coefficients of the semiempirical

Baumbach-Allen formula to 12 physical parameters in the framework of our DEM model (using eq. [7]),

$$n_e(R) = \sum_{i=1}^3 \int \frac{n_i}{\sqrt{2\pi\sigma_{T_i}}} \times \exp \left[-\frac{(R-1)r_\odot}{q_{\lambda,i}\lambda_0 T} - \frac{(T-T_i)^2}{2\sigma_{T_i}^2} \right] dT, \quad (21)$$

where the summation $i = 1, 2, 3$ represents the three coronal components (K, L, and F coronae), each one specified by a base density n_i , a DEM temperature range $T_i \pm \sigma_{T_i}$, and a scale height ratio $q_{\lambda,i} = \lambda_{n,i}/\lambda_{T,i}$.

We have found that the Baumbach-Allen formula is fully consistent with our DEM model, where every magnetic field line has a constant temperature with height, $T_e(h)$, while the height variation of the EM-weighted temperatures $T_{\text{EM}}(h)$ can naturally be explained by the multi-scale height weighting effects of a broad DEM distribution. This result stands in marked contrast to the finding of an apparent coronal temperature maximum at a height of $0.5 \lesssim h \lesssim 2 r_\odot$, as suggested by the scale height temperatures inferred from white-light inversions with the Baumbach-Allen formulation (Guhathakurta et al. 1999; Gibson et al. 1999). Our analysis invites the question of whether the latter finding is a side effect of the underlying model assumptions of hydrostatic equilibrium and isothermality (along each line of sight). This issue has crucial implications for coronal heating and solar wind acceleration models (e.g., Hansteen et al. 1997; Hansteen, Leer, & Lie-Svendsen 1999).

6. SUMMARY AND CONCLUSIONS

We analyzed quiet-Sun observations from 1992 August 26 obtained by *Yohkoh*/SXT, which are unique with regard to (1) long exposure times, (2) wide fields of view by off-pointing, and (3) minimum stray light. In a total of 35 radial sectors (with 10° width in position angle each) we model the soft X-ray fluxes as a function of height, in order to extract the radial density $n_e(h)$ and temperature profiles $T_e(h)$ in coronal holes, quiet-Sun regions, coronal streamers, and active regions.

Our approach differs from previous analytic methods, which are generally based on filter ratio temperatures and electron densities derived from the corresponding single-temperature emission measures. Instead, we parameterize our model with a DEM distribution $d\text{EM}(h, T)/dT$, which includes also a temperature dependence of density scale heights, $\lambda_n(T) = q_\lambda \lambda_0 T$. This model allows us to model hydrostatic atmospheres ($q_\lambda = 1$) as well as deviations from hydrostatic equilibrium ($q_\lambda \neq 1$). We calculate the line-of-sight integration in such multi-scale height atmospheres and convolve the DEM distributions with the instrumental response functions, yielding analytical expressions that can then be fitted to *Yohkoh*/SXT data with a numerical forward-fitting method. The model fitting provides solutions of four physical parameters: the DEM peak temperature T_0 , the (Gaussian) DEM temperature width σ_{T_0} , the coronal base electron density n_0 , and the scale height factor q_λ . The DEM distribution is characterized with a single Gaussian function, which adequately describes the plasma contributions in the temperature range of $\approx 0.5\text{--}5.0 \text{ MK}$, and thus allows for a self-consistent modeling of EUV, SXR, and white-light data. The major results of our analysis are as follows:

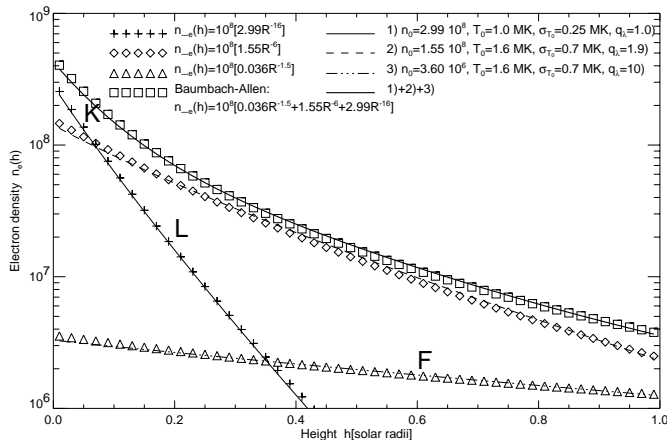


FIG. 12.—Baumbach-Allen formula $n_e(h)$ (*squares*) and its power-law components, associated with the K corona (*crosses*), the L corona (*diamonds*), and the F corona (*triangles*). Approximate fits to these three components and the sum (i.e., Baumbach-Allen formula) are shown with different line styles, and the fit parameters (n_0 , T_0 , σ_{T_0} , q_λ) are listed in the top part of the figure.

1. In *coronal holes* we find base densities of $n_0 \approx (0.8-1.1) \times 10^8 \text{ cm}^{-3}$, base temperatures of $T_0 = 1.3 \text{ MK}$ and $\sigma_{T_0} = 1.0 \text{ MK}$, and hydrostatic scale height factors of $q_\lambda \approx 1.0 \pm 0.2$. Thus, we find that coronal holes are in perfect hydrostatic equilibrium. The coronal hole densities are in good agreement with recent spectral line (Si XIII, Si IX, Mg IX, Mg X) measurements (e.g., Doschek et al. 1997; Guhathakurta et al. 1999) but are generally somewhat lower than density measurements inferred from white-light polarized brightness inversion, in a height range of $0.02 \lesssim h \lesssim 0.2 r_\odot$. However, our SXR-inferred densities seem to be in better agreement with solar wind models than white-light-inferred densities in the interface between chromospheric boundaries and the lower corona. Our DEM model can reproduce the positive temperature gradient with height, $dT_e(h)/dh > 0$, obtained by filter ratio temperatures. It can be entirely reproduced by the hydrostatic scale height weighting in a multitemperature atmosphere, where each magnetic field line is isothermal in itself.

2. In *quiet-Sun regions* we find base densities that are about a factor of 2 higher than in coronal holes, $n_0 = (1.9 \pm 0.8) \times 10^8 \text{ cm}^{-3}$; similar base temperatures $T_0 = 1.4 \text{ MK}$ and $\sigma_{T_0} = 1.0 \text{ MK}$; and also nearly hydrostatic scale height factors, $q_\lambda = 1.06 \pm 0.14$. Our density and temperature measurements are in reasonable agreement with previous quiet-Sun measurements in the height range of $h = 0.02-0.4 r_\odot$. Again, our DEM model can reproduce the positive temperature gradient seen by filter ratio temperatures without invoking a real temperature gradient along individual field lines.

3. In a *coronal streamer region* we find similar densities and temperatures as in quiet-Sun regions, but the most significant difference is that the scale height factor exceeds hydrostatic scale heights up to a factor of $q_\lambda = 2.3$ in the streamer center. This marked deviation from hydrostatic equilibrium strongly indicates the dynamic nature of coronal streamers. Our DEM model can reproduce the increase of the filter ratio temperature from $T_e = 1.8 \text{ MK}$ at the base of the streamer to $T_e = 2.8 \text{ MK}$ at an altitude of $h = 0.8 r_\odot$ with the same scale height weighting effect as found in other regions. Thus, the temperature structure of the streamer is consistent with a multitemperature bundle of near-isothermal field lines. We see no indication of a

temperature peak at a height of $h \approx 0.3 r_\odot$, as inferred from white-light inversions (Gibson et al. 1999). We suspect that this temperature peak is an artifact of the white-light inversion technique, which ignores deviations from hydrostatic equilibrium and neglects the multitemperature nature along the line of sight.

4. The *Baumbach-Allen formula*, which represents a semi-empirical model of the average coronal density as a function of height, $n_e(R)$, based on power-law approximations of three coronal components (K, L, and F coronae), can accurately be fitted by our DEM model and in this way provides additional physical information. From the fitting of our DEM model to the Baumbach-Allen formula we can confirm that the K corona is made of perfectly hydrostatic flux tubes with a DEM temperature distribution of $T_0 = 1.0 \text{ MK}$ and $\sigma_{T_0} = 0.25 \text{ MK}$; that the L corona consists of coronal streamers with a DEM temperature distribution of $T_0 = 1.6 \text{ MK}$ and $\sigma_{T_0} = 0.7 \text{ MK}$, with density scale heights that exceed the hydrostatic scale height by a factor of $q_\lambda \approx 1.9$; and that the F corona is far away from gravitational settling, as expected for interplanetary dust.

In conclusion, we think that the DEM approach represents a logical and clear concept to unify the analysis and interpretation of multiwavelength observations. In particular, it allows a treatment of density and temperature information in a self-consistent way, avoiding the inconsistencies that result from single-temperature approximations (such as filter ratios) and temperature-independent density modeling (such as white-light inversion techniques).

We would like to thank James Lemen, David Alexander, Nariaki Nitta, Hugh Hudson, Ruth Esser, and Harry Warren for helpful discussions and Dr. Viggo Hansteen for providing solar wind model data. We thank Dr. James Lemen for insightful guidance in *Yohkoh* data analysis. *Yohkoh* is a mission of the Japanese Institute for Space and Astronautical Science. This work is supported by NASA under contract NAS8-40108. The authors are grateful to the referee, Madhulika Guhathakurta, for help with the paper improvement.

REFERENCES

- Acton, L. W., & Lemen, J. R. 1998, in *Observational Plasma Astrophysics: Five Years of Yohkoh and Beyond*, ed. T. Watanabe et al. (Dordrecht: Kluwer), 15
- Ahmad, I. A., & Webb, D. F. 1978, *Sol. Phys.*, 58, 323
- Ahmad, I. A., & Withbroe, G. L. 1977, *Sol. Phys.*, 53, 397
- Alexander, D. 1999, *J. Geophys. Res.*, 104, 9701
- Allen, C. W. 1964, *Astrophysical Quantities* (London: Athlone)
- Aschwanden, M. J., Nightingale, R. W., & Alexander, D. 2000, *ApJ*, 541, 1059
- Aschwanden, M. J., & Nitta, N. 2000, *ApJ*, 535, L59
- Bohlin, J. D., Sheeley, N. R., Jr., & Tousey, R. 1975, in *Space Research Vol. 15*, ed. M. J. Rycroft (Berlin: Akademie), 651
- Brosius, J. W., Davila, J. M., Thomas, R. J., & Monsignori-Fossi, B. C. 1996, *ApJS*, 106, 143
- Del Zanna, G., & Bromage, B. J. I. 1999, *J. Geophys. Res.*, 104, 9753
- Dollfus, A., & Martres, N.-J. 1977, *Sol. Phys.*, 53, 449
- Doschek, G. A., Warren, H. P., Laming, J. M., Mariska, J. T., Wilhelm, K., Lemaire, P., Schühle, U., & Moran, T. G. 1997, *ApJ*, 482, L109
- Esser, R., & Sasselov, D. 1999, *ApJ*, 521, L145
- Feldman, U., Doschek, G. A., Schühle, U., & Wilhelm, K. 1999, *ApJ*, 518, 500
- Fisher, R., & Guhathakurta, M. 1995, *ApJ*, 447, L139
- Fludra, A., Del Zanna, G., Alexander, D., & Bromage, B. J. I. 1999, *Geophys. Res. Lett.*, 104, 9709
- Gallagher, P. T., Mathioudakis, M., Keenan, F. P., Phillips, K. J. H., & Tsinganos, K. 1999, *ApJ*, 524, L133
- Galvin, A. B., & Kohl, J. L. 1999, *J. Geophys. Res.*, 104, 9673
- Gibson, S. E., Fludra, A., Bagenal, F., Biesecker, D., Del Zanna, G., & Bromage, B. 1999, *J. Geophys. Res.*, 104, 9691
- Guhathakurta, M., & Fisher, R. 1998, *ApJ*, 499, L215
- Guhathakurta, M., Fludra, A., Gibson, S. E., Biesecker, D., & Fisher, R. 1999, *J. Geophys. Res.*, 104, 9801
- Guhathakurta, M., Rottman, G. J., Fisher, R. R., Orrall, F. Q., & Altrock, R. C. 1992, *ApJ*, 388, 633
- Habbal, S. R., Esser, R., & Arndt, M. B. 1993, *ApJ*, 413, 435
- Hansteen, V. H., Leer, E., & Holzer, T. E. 1997, *ApJ*, 482, 498
- Hansteen, V. H., Leer, E., & Lie-Svendsen, O. O. 1999, in *Proc. 9th European Meeting on Solar Physics, Magnetic Fields and Solar Processes* (Florence: ESA SP-448), 1091
- Koutchmy, S. 1977, *Sol. Phys.*, 51, 399
- Lallement, R., Holzer, T. E., & Munro, R. 1986, *J. Geophys. Res.*, 91, 6751
- Mariska, J. T. 1978, *ApJ*, 225, 252
- Press, W. H., Flannery, B. P., Teukolsky, S. A., & Vetterling, W. T. 1986, *Numerical Recipes, The Art of Scientific Computing* (Cambridge: Cambridge Univ. Press), 274
- Saito, K. 1965, *PASJ*, 17, 1
- . 1970, *Ann. Tokyo Astron. Obs.*, 12, 51
- Sturrock, P. A., Wheatland, M. S., & Acton, L. W. 1996, *ApJ*, 461, L115

- Tsuneta, S., et al. 1991, *Sol. Phys.*, 136, 37
- van de Hulst, H. C. 1950a, *Bull. Astron. Inst. Netherlands*, 11, 135
- , 1950b, *Bull. Astron. Inst. Netherlands*, 11, 150
- Wheatland, M. S., Sturrock, P. A., & Acton, L. W. 1997, *ApJ*, 482, 510
- Wilhelm, K., Marsch, E., Dwivedi, N., Hassler, D. M., Lemaire, P., Gabriel, A. H., & Huber, M. C. E. 1998, *ApJ*, 500, 1023
- Wolfson, R., Roald, C. B., Sturrock, P. A., Lemen, J., & Shirts, P. 2000, *ApJ*, 529, 570
- Zhang, J., White, S. M., & Kundu, M. R. 1999, *ApJ*, 527, 977
- Zidowitz, S. 1999, *J. Geophys. Res.*, 104, 9727